

# Radio-Excess *IRAS* Galaxies: IV. Optical Spectroscopy

Catherine L. Buchanan<sup>\*,1,2</sup>, Peter J. McGregor<sup>1</sup>, Geoffrey V. Bicknell<sup>1</sup>,  
and  
Michael A. Dopita<sup>1</sup>

clbps@cis.rit.edu, peter,geoff,mad@mso.anu.edu.au

## ABSTRACT

This is the fourth in our series of papers discussing the nature of radio-excess galaxies, which have radio emission associated with an active nucleus but which do not fit into the traditional categories of either radio-loud or radio-quiet active galaxies. In this paper, we present optical spectra of our sample of FIR-luminous radio-excess galaxies. Optical emission line ratio diagnostics are used to determine the dominant source of the ionizing radiation. We find that radio excess is an excellent indicator of the presence of an active nucleus. The radio-excess sample contains a much higher fraction of AGN than samples selected on FIR luminosity alone, or using other criteria such as warm FIR colors. Several objects have ambiguous classifications and are likely to be composite objects with mixed excitation. The type of optical spectrum appears to be associated with the radio-loudness: our results suggest that radio-loud objects may be more ‘pure’ AGN than radio-intermediate objects. We find strong evidence for interaction between the radio plasma and the surrounding gas. Broad, structured optical emission lines are observed and a relative blueshift is measured between the [O III]  $\lambda 5007$  and  $H\alpha$  lines in several sources. Jet energy fluxes are inferred from the [O III]  $\lambda 5007$  luminosities using a shock model for the interaction between the radio jet and the line-emitting gas. The jet energy fluxes of the radio-excess objects are lower than in powerful radio sources, consistent with our previous results. We conclude that the jets of radio-intermediate sources are intrinsically weaker than those in sources with more powerful radio emission. A significant fraction of the sample spectra show post-starburst stellar continuum, with A-star absorption lines. Post-starburst stellar populations are consistent with the large fraction of merging or disturbed host galaxies in the sample. The ages of the radio sources are significantly less than those of A stars indicating that, if the radio sources are associated with merging activity, there is a delay between the interaction and the initiation of the radio activity.

*Subject headings:* galaxies: active — galaxies: Seyfert — infrared: galaxies — radio continuum: galaxies — galaxies: jets

## 1. Introduction

Optical emission lines are a characteristic feature of active galaxies. The ionizing source for the optical emission lines seen in AGN is a combina-

tion of photoionization by ultraviolet (UV) continuum emission from the nucleus and shock ionization produced by high velocity outflows such as radio jets. In powerful radio galaxies, the optical emission lines reveal the interaction between the radio plasma and the surrounding medium. Detailed studies of individual radio galaxies suggest that the radio and line-emitting regions are spatially coincident and reveal kinematic evidence for shocks and acceleration of the line-emitting material by the jet and overpressured lobes (e.g., van

<sup>\*</sup>Previously Catherine L. Drake

<sup>1</sup>Research School of Astronomy and Astrophysics, The Australian National University, Cotter Rd, Weston, ACT 2611 Australia

<sup>2</sup>Now at Rochester Institute of Technology, 84 Lomb Memorial Drive, Rochester NY 14623-5603 USA

Breugel et al. 1984a,b; Tadhunter 1991; Koekemoer & Bicknell 1998; Villar-Martín et al. 1999; Solórzano-Iñarrea et al. 2001, 2002; Koekemoer & Bicknell 2002).

Studies of samples of radio galaxies have shown that the interaction between the radio plasma and the surrounding medium is related to the radio source size (Best, Röttgering, & Longair 2000, Best et al. 2002; Inskip et al. 2002b). These results have shown that radio plasma/cloud interactions dominate the kinematics and ionization of the line-emitting material while the source is young and expanding through the interstellar medium of the host galaxy. In more evolved radio sources, with larger extents, the line-emitting material is predominantly photoionized by the central ultraviolet continuum source, and the kinematics are consistent with gravitational motion in the host galaxy potential. The radio plasma interactions may take the form of direct jet–cloud interactions or interactions with the over–pressured radio lobe.

Powerful compact radio sources that are embedded in the dense inner regions of the host galaxy show evidence for strong interaction between the expanding radio lobes and the interstellar medium. Gelderman & Whittle (1994) discovered broad, complex line profiles in compact-steep spectrum (CSS) sources. A detailed study of three CSS sources found broad emission line widths, complex line profiles, and velocity offsets in the emission line gas surrounding the radio sources (O’Dea et al. 2002, 2003). The [O III]  $\lambda 5007$  emission line in two other CSS sources has been shown to be blueshifted by 600 – 2000 km s<sup>−1</sup> with respect to the systemic velocity of the host and low ionization lines (Holt et al. 2003; Tadhunter et al. 2001). These studies provide strong evidence for acceleration of the line-emitting gas by powerful radio jets. Some evidence has also been found for interaction between the much weaker radio sources found in Seyfert galaxies and the surrounding medium (Whittle 1992b).

The radio continuum and [O III]  $\lambda 5007$  line luminosities are found to be correlated in samples of radio galaxies (e.g., Baum & Heckman 1989; Rawlings & Saunders 1991; Tadhunter et al. 1998; Baum & McCarthy 2000). This suggests either a direct relation between the radio jets and the line emission, or that both are directly related to the luminosity of the central engine. A correla-

tion between the radio power and [O III]  $\lambda 5007$  emission is also seen in Seyfert galaxies (de Bruyn & Wilson 1978; Whittle 1985). This correlation is separated from the radio galaxy correlation by approximately four orders of magnitude in radio power and this has been used to argue for a dichotomy between radio-loud and radio-quiet AGN (Wilson & Colbert 1995). The correlation between radio power and [O III]  $\lambda 5007$  luminosity in Seyfert galaxies is most likely due to the relation both have with the properties of central engine, although the physical details of this correlation remain to be elucidated.

In this paper we investigate the optical spectroscopic properties of our sample of 49 FIR-luminous radio-excess galaxies, and the hypothesis that they resemble low-power CSS/GPS sources. The spectroscopic observations and measurements are described in §2. The line ratios and object classifications as well as line widths and equivalent widths are presented in §3. In §4 we discuss the classifications and the [O III]  $\lambda 5007$  luminosities of the radio-excess objects as a function of their radio power. We use models to infer properties of the radio jets from the optical line emission, and discuss the presence of stellar continuum and absorption lines in sample spectra. Our conclusions are presented in §5. For consistency with our previous work, we adopt the cosmological parameters  $H_0 = 50$  km s<sup>−1</sup>Mpc<sup>−1</sup> and  $q_0 = 0.5$ .

## 2. Optical spectroscopy

The selection of the radio-excess sample is described in detail in Drake et al. (2003, hereafter Paper I). Briefly, objects were found by cross-correlating the Parkes-MIT-NRAO 5 GHz radio source catalog (Griffith & Wright 1993; Griffith et al. 1994; Wright et al. 1994; Griffith et al. 1995; Wright et al. 1996) with the *IRAS* FSC (Moshir et al. 1992). Objects having more than 5 times as much radio emission as expected from the far-infrared/radio correlation followed by star-forming galaxies and radio-quiet active galaxies were selected to form the radio-excess sample. This criterion corresponds to  $\log [S_\nu(60 \mu\text{m})/S_\nu(4.8 \text{ GHz})] < 1.80$ . The FIR-luminous subsample selected for further study comprises those radio-excess objects with  $\nu L_\nu(60 \mu\text{m}) > 10^{11} L_\odot$ . This selection is

described in Drake et al. (2004a, hereafter Paper II). The FIR-luminous radio-excess objects were observed with the Double-Beam Spectrograph (DBS) on the Australian National University (ANU) 2.3 m telescope at Siding Spring Observatory. The B300 and R316 gratings were used in the blue and red arms, respectively, giving a spectral resolution of  $\sim 5 \text{ \AA}$ . The observations and reduction of the spectra are described in detail in Paper I. The low resolution optical spectra are shown in Appendix A, Figures 14a - m. Some of the objects were observed again with the B600 and R600 gratings of the DBS, at a spectral resolution of  $\sim 2 \text{ \AA}$ . These spectra were reduced by the same method as the lower resolution spectra.

Spectrophotometric measurements were performed on the lower resolution spectra using the *IRAF* data reduction package. The line fluxes and widths of unblended lines were measured by Gaussian fitting using the SPLOT task. At the resolution of the observations, several emission lines were blended, including  $H\alpha$  with [N II]  $\lambda 6548$ ,  $6584$  and [S II]  $\lambda 6717$  with [S II]  $\lambda 6731$ . Parameters for these lines were measured by simultaneously fitting multiple Gaussians using the task NGAUSSFIT. This task allows the widths and fluxes of lines of the same species to be fixed relative to each other. Where  $H\beta$  was present in both absorption and emission, NGAUSSFIT was used to fit these simultaneously. For eight objects the  $H\alpha$  and  $H\beta$  emission was fitted with a broad as well as a narrow component. The line flux in these cases is listed as the sum of the two components but the line ratios were calculated using the narrow component only.

The line fluxes were corrected for reddening following Veilleux & Osterbrock (1987). The  $H\alpha$  and  $H\beta$  lines were used to determine the Balmer decrement, and the Whitford reddening curve was used to determine the reddening (Miller & Mathews 1972). An intrinsic flux ratio of  $H\alpha/H\beta = 3.1$  was assumed for all objects. This value is slightly higher than the Case B Balmer recombination ratio of 2.85 expected for starburst galaxies and is more appropriate for active galaxies (Veilleux & Osterbrock 1987), however we note that the object classifications (§3) are unchanged if an intrinsic  $H\alpha/H\beta = 2.85$  is used for the reddening correction. The (uncorrected)  $H\alpha$  and  $H\beta$  fluxes, along with the derived extinction, are listed in Ta-

ble 1. The fluxes of other emission lines, corrected for reddening, are listed in Table 2. Where  $H\beta$  is an upper limit, the reddening estimate is a lower limit. Two spectra had no  $H\alpha$  emission line; no reddening was calculated for these spectra.

The line widths were taken to be the full width at half-maximum (FWHM) of the fitted Gaussian. The instrumental broadening was measured by fitting Gaussian profiles to emission lines in sky spectra extracted from the same image as the object spectrum. These were typically  $\sim 5.0 \text{ \AA}$ . The instrumental FWHM was subtracted in quadrature from each measured line width to estimate the intrinsic line width. These are listed in Table 3. Equivalent widths of the emission lines were derived from the fitted Gaussian profiles using the SPLOT task. The equivalent width of the [O III]  $\lambda 5007$  emission line for each spectrum is listed in Table 4.

### 3. Results

Reddening-corrected narrow-line ratios were derived and plotted on three Veilleux & Osterbrock (1987) diagnostic diagrams to determine the nature of the line-emitting region (see Figure 1). The theoretical scheme of Kewley et al. (2001) was used to classify the galaxies into starbursts (SB), Seyferts (Sy), and low-ionization narrow emission-line region (LINER) galaxies. This scheme has been shown to give similar results to the semi-empirical scheme of Veilleux & Osterbrock (1987), but with fewer ambiguous classifications (Kewley et al. 2001; Corbett et al. 2003). Objects below and to the left of the maximum starburst (*solid*) line on each diagram are classified as SB. Objects above this line and to the left of an extreme mixing line (*solid line*) are classified as Sy. The mixing line indicates the locus of objects with a maximum starburst combined with 0 - 100% contribution by an AGN component. Objects above the maximum starburst line and to the right of the extreme mixing line are classed as LINERs. Objects were classified by their location in the three diagnostic diagrams. In most cases the three classifications agreed and a final type was assigned to the object. Objects for which the three classifications did not agree are described as ambiguous. The classifications and assigned types are listed in Table 5.

The diagnostic diagrams (Figure 1) reveal that the majority of the objects have Seyfert spectra. We find 27 galaxies with Seyfert spectra (75%) and one galaxy with a starburst spectrum (3%). No objects were unambiguously classified as LINERs. The remaining eight objects (22%) had ambiguous classifications. Of these, five were Sy/LINER, one was SB/LINER and one was Sy/SB/LINER. The Seyfert galaxies were further divided into broad- and narrow-line objects (Seyfert types 1 and 2) based on the  $H\alpha$  line widths (Table 3). Seyferts with  $\text{FWHM}_{H\alpha} > 2000 \text{ km s}^{-1}$  were classified as Sy 1 and objects with narrower  $H\alpha$  emission lines as Sy 2.

We extracted fixed-size apertures for all sample objects. Veilleux (2002) noted that aperture effects can cause line ratios to move towards the starburst region of the diagram, when the same sized aperture is used for objects of different redshifts. This occurs because the corresponding linear aperture is larger for higher redshift objects and starburst regions often surround the nucleus. The potential contamination from any circumnuclear starburst increases with redshift. The extracted apertures (12 pixels  $\sim 10''$ ) correspond to scales of  $\sim 10 - 70 \text{ kpc}$  at the redshifts of our objects. However we see no evidence that objects with higher redshifts lie closer to the starburst region than lower redshift objects.

## 4. Discussion

### 4.1. Classifications

Classifying objects based on the diagnostic diagrams, we find the majority of objects in the sample (75%) are AGN. Using the theoretical scheme of Kewley et al. (2001), we find that 56% of the objects are Seyfert type 2 and 19% are Seyfert type 1 ( $\text{FWHM}_{H\alpha} > 2000 \text{ km s}^{-1}$ ). Only one object is classified as a starburst and no object is classified as a LINER. Classifications for eight objects (22%) were ambiguous. These objects are discussed further below.

We find a higher fraction of AGN than in samples of objects selected on FIR luminosity alone, which are dominated by radio-quiet objects at *IRAS* flux densities. This confirms that the radio-excess criterion selects AGN (see Paper I). Studies with other selection criteria, aimed at selecting AGN, have also found a higher fraction of AGN,

though none of these contain as high a fraction as found in our sample. For example, de Grijp et al. (1992) selected IR galaxies with warm FIR colors and found 22% Seyfert 1, 39% Seyfert 2 galaxies and 37% starburst galaxies. Samples selected only on FIR luminosity find lower fractions of AGN and higher fractions of starburst and LINER galaxies. In their sample of luminous infrared galaxies, Veilleux et al. (1995) found 12% of their objects were Seyfert 2 and only 2% were Seyfert 1, while 59% of the sample were SB and 27% were LINER galaxies. Kewley et al. (2001) found a similarly low fraction of AGN and high fraction of starbursts in their sample of largely radio-quiet IR-luminous galaxies. They find only 0.4% of LINERs in their sample. Some of this difference may also be attributable to different classification methods, especially for the LINERs. Veilleux et al. (1995) use the criterion  $\log [\text{O III}]/H\beta \leq 3$  to classify LINERs, while Kewley et al. (2001) use the criteria we adopted. Kewley et al. (2001) note that 6% of galaxies in their sample are classified as LINERs using the criteria of Veilleux et al. (1995). We find that five objects with ambiguous classifications and one object classified as a Seyfert, in total 12% of our sample, have  $\log [\text{O III}]/H\beta \leq 3$ .

Figure 2 shows the diagnostic diagrams with symbols indicating the level of radio-excess of the object. Following Paper I, we have divided the sample into radio-intermediate ( $0.0 < u < 1.80$ ) and radio-loud ( $u < 0.0$ ) objects, where the radio-excess parameter  $u = \log [S_\nu(60 \mu\text{m})/S_\nu(4.8 \text{ GHz})]$ . There is a clear tendency for the radio-loud objects (*open circles*) to be higher up the mixing line derived by Kewley et al. (2001) and so exhibit a higher percentage of pure AGN excitation than the radio-intermediate objects. The Kaplan-Meier estimator shows the means of the  $\log [\text{O III}]/H\beta$  for the radio-intermediate and radio-loud objects to be  $0.78 \pm 0.07$  and  $1.05 \pm 0.07$ , respectively. However, two-sample Gehan and logrank tests using survival analysis methods to account for lower limits indicate differences in  $\log [\text{O III}]/H\beta$  between the radio-intermediate and radio-loud objects with significance levels of only  $\sim 10\%$ . A larger sample is required to investigate properly the relation between the radio loudness and the properties of the optical spectrum. The radio-intermediate objects are less powerful AGN in both the radio and the optical, compared with

the radio-loud objects, so it may be that the radio-intermediate objects have a composite excitation containing a higher fraction of starburst contribution.

One object is classified as starburst on the diagnostic diagrams. This object, F21139-6613, falls quite close to the maximum starburst line in Figure 1, within the uncertainties, in two of the three diagrams. It has a modest radio excess ( $u = 1.2$ ) and high FIR luminosity ( $\log \nu L_\nu(60 \mu\text{m}) = 11.7 L_\odot$ ). It has the highest extinction of any object in the sample, with  $E(B-V) = 3.1$ . It is therefore likely to be a composite starburst-AGN in which the AGN is highly reddened and consequently obscured at optical wavelengths.

Several of the ambiguous classifications can be redefined as borderline rather than ambiguous, as the objects lie very close to the borders between regions in one or more diagrams. The eight objects with ambiguous classifications tend to have large uncertainties in their line ratios. These objects may also be composite starburst/AGN in which nuclear activity is either weak or highly obscured.

Figure 3 shows the FIR color-color diagram for the objects with measured *IRAS* 25  $\mu\text{m}$  and 12  $\mu\text{m}$  fluxes (Paper I). While the majority of objects with unambiguous classifications do not have measured *IRAS* fluxes in these bands, the few objects that can be plotted are mostly Seyferts that fall along the reddening line (Dopita et al. 1998). Thus the optical diagnostics and FIR colors of these objects agree, suggesting that these are highly reddened Seyfert galaxies. The location of the three ambiguous objects on this diagram is consistent with these being composite and/or highly obscured objects.

#### 4.2. Jet/ISM Interaction

Most of the FIR-luminous radio-excess objects show broad [O III]  $\lambda 5007$  line widths. The distribution of measured line widths for our objects, corrected for instrumental broadening, are shown in Figure 4 (*top panel*). Data from the literature for other objects are shown for comparison. The line widths of the FIR-luminous radio-excess galaxies cover a broad range of velocities from as narrow as  $\sim 250 \text{ km s}^{-1}$  to almost  $2000 \text{ km s}^{-1}$ . The line widths are broader than typical galaxian rotation, suggesting that there is

strong interaction between the radio source and the line-emitting gas in the radio-excess objects. The line widths are similar to CSS sources and broader than observed in extended radio galaxies and Seyferts with linear radio sources.

Broad line widths have been observed in powerful compact radio sources and interpreted to indicate strong interaction between the radio jet and the host ISM (e.g., Gelderman & Whittle 1994; O’Dea et al. 2002, 2003). Whittle (1992b) has shown that the line widths of radio-quiet Seyfert galaxies correlate with the rotational velocity of the galaxy, and that Seyfert galaxies with linear radio sources have broader line widths. The kinematics of the narrow-line region in radio-quiet galaxies therefore seems to be dominated by the galaxy potential. The cited work indicates that in those objects with linear radio sources, the interaction of the radio plasma with the line-emitting material accelerates the gas and produces broader line widths. In the case of powerful radio galaxies, the line widths are not as broad as in CSS sources because the radio jets do not interact as strongly with the gas in the narrow-line region. The powerful radio galaxies show similar line widths to the Seyfert galaxies. However, all except one of the high-redshift radio galaxies ( $z > 0.6$ ; *filled histogram, middle panel*) fall at the upper end of the distribution, with the broadest line widths. Baum & McCarthy (2000) note this difference between the low- and high-redshift objects in their sample. If broad line widths in these objects are attributable to interaction between the radio source and the surrounding gas, the increase in line width with redshift can be interpreted as an increase in strength of the interaction with radio power. Alternatively, Baum & McCarthy (2000) argue that if the broad line widths are associated with larger gravitational potentials, the increase in line width with redshift indicates that the environment of radio galaxies changes with redshift. Thus part of the correlation may simply be an environmental effect. Recent studies suggest that both effects are operating; radio sources interact more strongly with the environment when they are small and expanding into the dense host galaxy medium, and more extreme kinematics are observed at higher redshift as a result of different environments (Best et al. 2000, 2002; Inskip et al. 2002a,b).

ULIRG Seyferts show a large range of line

widths, some as broad as those in our sample. Little is known about the radio properties of these objects, but at least four are known to be radio-excess objects, including two objects that are also present in our sample. These four objects all have broad line widths (Figure 4; *filled histogram, bottom panel*). The ULIRG Seyferts would seem to comprise both radio-quiet objects in which the [O III]  $\lambda$ 5007 line width reflects the galaxian rotation, and radio-excess objects, in which there is additional acceleration of the line-emitting material by the radio plasma.

We do not detect any correlation of the [O III]  $\lambda$ 5007 line width with the radio power (Figure 5). This is consistent with the similar line widths seen between the radio-excess galaxies and the more powerful CSS/GPS sources and suggests that the radio power is not the dominant factor determining the amount of line broadening. Other factors, such as the amount of gas in the narrow-line region, may be more important.

We find further evidence for acceleration of the line-emitting material in some objects. In six galaxies we detect a blueshift between the [O III]  $\lambda$ 5007 and H $\alpha$  emission lines. These are shown in Figure 6. Blueshifts between forbidden and permitted lines have previously been observed in two objects in our sample that have compact powerful radio sources, including F15494-7905, shown in Figure 6 (Holt et al. 2003; Tadhunter et al. 2001). They have been interpreted as evidence for outflows, where the permitted lines are at the systemic velocity of the galaxy and the forbidden lines are produced in gas that is being accelerated and shock-excited by the radio jet or expanding lobe. The objects with blueshifts all have broad [O III]  $\lambda$ 5007 line widths, but they have radio powers and radio excesses covering the full range in the sample. Thus, such outflows are not associated exclusively with objects having high radio powers. Complex line profiles are also seen in some objects. Figure 7 shows the [O III]  $\lambda$ 5007 profiles of two objects observed at higher resolution. Complex line profiles have been observed in powerful radio sources and Seyfert galaxies with linear radio sources and indicate that the radio jet that is accelerating the surrounding material produces complex kinematics in the line-emitting regions (Gelderman & Whittle 1994; Whittle 1992b).

### 4.3. Jet Energy Fluxes

The radio-excess objects were selected in such a way that they include many objects that lie between radio-loud and radio-quiet objects in their radio/FIR flux density ratios. We find that many of these are also intermediate in their ratio of radio to [O III]  $\lambda$ 5007 line luminosity. Figure 8 shows the distributions of this ratio for the FIR-luminous radio-excess sample and radio-loud together with radio-quiet objects from the literature for comparison. The radio-excess objects fall between powerful radio sources and Seyfert galaxies in their ratio of [O III]  $\lambda$ 5007 luminosity to radio power, filling the gap between the distributions of the radio-loud and radio-quiet objects.

We find that the radio-excess galaxies have [O III]  $\lambda$ 5007 emission lines as luminous as those in powerful radio sources, but that they lie between radio-loud objects and radio-quiet objects on the  $L_{[\text{O III}] \lambda 5007} - P_{4.8 \text{ GHz}}$  diagram. Figure 9 shows the [O III]  $\lambda$ 5007 emission line luminosity relative to the radio power for the radio-excess sample and the comparison radio-quiet and radio-loud objects. Independent correlations have been observed between the radio power and [O III]  $\lambda$ 5007 luminosity in radio-quiet (de Bruyn & Wilson 1978; Whittle 1985) and radio-loud sources (Baum & Heckman 1989; Rawlings & Saunders 1991; Tadhunter et al. 1998; Baum & McCarthy 2000). Two hypotheses to explain these correlations have been investigated: photoionization by a central UV continuum source, or shock ionization by the radio jets. Evidence for both has been found. Baum & McCarthy (2000) found that the emission-line luminosities in their sample of 52 3CR radio galaxies were proportional to the nuclear UV continuum flux densities, suggesting that photoionization is the dominant ionization mechanism. However, their results did not exclude ionization by shocks. Several detailed studies of individual objects have found morphological similarities between radio and line-emitting regions and kinematic evidence for shocks (e.g., van Breugel et al. 1984a,b; Tadhunter 1991; Koekemoer & Bicknell 1998; Villar-Martín et al. 1999; Solórzano-Iñarrea et al. 2001, 2002; Koekemoer & Bicknell 2002). The alignment of line-emitting regions with the axis of the radio jet in high-redshift radio galaxies has been interpreted as evidence for an anisotropic UV source and for shock-induced continuum by

the radio jet (Baum & McCarthy 2000; Best et al. 1999). Given that there is evidence for both mechanisms, it is likely that the observed emission results from a combination of photoionization and shock ionization. A number of studies have shown that shock ionization is more important in smaller radio sources, confined within the optical extent of the host galaxy, while the emission-line regions in larger sources are predominantly photoionized (Best et al. 1999, 2002; Inskip et al. 2002a,b). The broad line widths in CSS sources support the hypothesis that the radio jet produces radiative shocks in a dense interstellar medium (Gelderman & Whittle 1994). Thus in the compact radio-excess objects, we expect shocks to play a large role in producing the optical line emission. However, in radio-quiet Seyfert galaxies that have no radio jets the optical line emission is likely to be predominantly photoionized by ultraviolet photons from the active nucleus. The [O III]  $\lambda 5007$  emission in the radio-excess objects may therefore include a significant photoionized component. In some objects, which have strong stellar continuum, there may also be a contribution associated with star formation. The lack of any trend of [O III]  $\lambda 5007$  line width with radio power (Figure 5) suggests that a combination of ionization mechanisms is operating. The line width is bounded at the lower limit by the gravitational motions of the galaxy, and at the upper limit by the condition that the shocks are radiative. The distribution of points in Figure 5 indicates that most objects are of mixed excitation.

The radio and optical line emission of compact radio sources have been modeled by Bicknell, Dopita, & O’Dea (1997). The model describes the evolution of a jet-fed radio lobe as it expands into the dense interstellar medium. In the Bicknell et al. model the total shock luminosity is equated to the rate of work done on the surrounding medium by the expansion of the lobe. This leads to the following relation between the [O III]  $\lambda 5007$  luminosity,  $L_{[\text{O III}] \lambda 5007}$ , and the jet energy flux,  $F_E$ .

$$L_{[\text{O III}] \lambda 5007} \sim 1.0 \times 10^{-2} \left( \frac{6}{8 - \delta} \right) F_E \text{ erg s}^{-1}, \quad (1)$$

where the density of the surrounding medium varies as  $R^{-\delta}$ ,  $R$  being the distance from the nucleus. We assume  $\delta = 1.5$ . This relation underesti-

mates the jet energy flux if the medium is clumpy. In the case of GPS and CSS sources, the expansion speeds  $\sim 0.1 - 0.4 c$  of the radio plasma indicate that the filling factor of dense clouds in the interstellar medium is relatively low (Conway 2002; Murgia et al. 1999; Parma et al. 1999; Murgia et al. 2002; Murgia 2003; Owsianik & Conway 1998; Owsianik, Conway, & Polatidis 1999). However, in the case of our radio-excess objects, which show evidence of more recent interaction or merging activity, the medium may not be as clumped. This is consistent with the modest radio lobe expansion velocities ( $\lesssim 0.01 c$ ) inferred in Drake et al. (2004b, hereafter Paper III), and we comment further on this below. We assume that the optical line emission in the radio-excess objects is predominantly shock-excited, and thus this model may be used to infer the radio jet energy flux from the [O III]  $\lambda 5007$  luminosity. If there is a significant contribution from photoionization or star formation, the derived properties of the radio jets are overestimates. The [O III]  $\lambda 5007$  luminosities and the jet energy fluxes, derived from Equation 1, are listed in Table 6. The jet energy fluxes are lower than for powerful radio sources, consistent with the results of Paper III, where we estimated jet energy fluxes from the radio spectral energy distributions of several radio-excess sources. Objects with the highest radio powers also have the highest [O III]  $\lambda 5007$  luminosities. Thus the radio-loud objects (those with  $u < 0$ ) have the highest jet energy fluxes, and objects with more moderate radio excesses tend to have lower jet energy fluxes.

Let us examine these estimates for the energy flux in the light of the velocity estimates of Paper III. Using equation (2.10) and (2.12) of Bicknell, Dopita, & O’Dea (1997), the velocity of expansion of a radio lobe of size  $x_h$  in a smooth medium with Hydrogen number density,  $n_H$  is given by:

$$V_c \simeq 1500 \text{ km s}^{-1} \left( \frac{6}{8 - \delta} \right)^{1/3} \times \zeta^{1/6} \left( \frac{F_{E,45}}{n_H(\text{kpc})} \right)^{1/3} \left( \frac{x_h}{\text{kpc}} \right)^{(\delta-2)/3} \quad (2)$$

where  $\zeta \simeq 2$ , and  $F_{E,45}$  is the jet energy flux in units of  $10^{45} \text{ erg s}^{-1}$ . Thus, the expansion velocities estimated in Paper III are consistent with  $F_{E,45}/n_H(\text{kpc}) \sim 1$ . In view of our energy flux

estimates, this implies that  $n_H(\text{kpc}) \sim 1$ ; for a temperature  $\sim 10^7$ , the corresponding  $p/k \sim 10^7$ .

The energy fluxes in our radio-excess objects are much less than that in GPS and CSS sources (Bicknell, Saxton, & Sutherland 2003), yet the [O III] fluxes are similar. Figure 8 shows the distribution of [O III]  $\lambda$  5007 luminosity to radio luminosity and it is clear that this parameter is systematically higher for the radio excess objects compared to GPS and CSS sources. This requires comment. There are two important effects to take into account: (1) The lower expansion velocities of radio-excess objects mean that it is easier for the shocks to be radiative in the sense that the radiative timescale should be less than the dynamical time scale. (See Bicknell, Dopita, & O’Dea 1997 and Bicknell, Saxton, & Sutherland 2003 for discussions of this point.) (2) The covering factor of dense clouds may be larger, consistent with our assumption of a medium with a higher filling factor.

#### 4.4. Continuum Emission

A number of objects show strong continuum as well as emission lines in their spectra. In the case of a few, with broad emission lines, the continuum is likely to be associated with the central nucleus. However other objects show strong stellar continuum and absorption lines that indicate the nature of the dominant stellar population in the host galaxy. A substantial fraction of the sample spectra show absorption indicative of an intermediate age stellar population. Sixteen objects (33%) show  $H\beta$ , or  $H\gamma$ ,  $H\delta$ , and  $H\epsilon$  absorption. The stellar continuum and absorption in these objects are typical of A type stars. Objects with this type of optical spectrum have previously been described as post-starburst AGN (Dey & van Breugel 1994). They are composite objects that are believed to have undergone a starburst within the past  $\sim 10^8$  years, and that are now dominated by an intermediate-age stellar population and an active nucleus. A further 13 objects in the sample (27%) show redder stellar continuum and absorption typical of elliptical galaxies. These objects resemble normal radio-loud objects for which the AGN host galaxies are luminous elliptical galaxies.

Figure 10 shows the equivalent widths of the [O III]  $\lambda$ 5007 emission lines as a function of [O III]  $\lambda$ 5007 luminosity. The symbols indicate

the type of stellar population, either A-star (*open stars*), or old elliptical stellar population (*filled circles*). Also plotted are objects showing minimal stellar continuum in their spectrum (*x’s*), for which the nature of the underlying continuum cannot be established. The equivalent widths and luminosities of the [O III]  $\lambda$ 5007 emission lines show a correlation because the range of continuum luminosities in the sample is narrow compared with the range of line luminosities. Figure 10 shows that the objects with minimal stellar continuum all have high equivalent widths and luminous [O III]  $\lambda$ 5007 emission. In contrast, the objects with A-star stellar continuum have low to moderate [O III]  $\lambda$ 5007 equivalent widths and luminosities. Objects with an older stellar population, typical of elliptical galaxies, have intermediate equivalent widths and luminosities.

The distribution of points on this diagram may indicate that there are different types of objects in the sample; post-starburst galaxies and ellipticals with higher intrinsic luminosities. Alternatively, it may reflect different ages of objects in the sample, indicating an aging sequence from post-starburst galaxy to evolved elliptical to AGN. In the first case, we would expect the different types of object to have different host morphologies. In the second case, we would expect the morphological type of the host galaxy to be unrelated to the location of each object in Figure 10. We show in Figure 11 the [O III]  $\lambda$ 5007 equivalent widths and luminosities plotted with different symbols indicating the host morphological type determined in Paper II. Morphological types determined by surface-brightness fitting were disks (*open circles*) and ellipticals/bulges (*filled squares*), point sources (*star*), and undetermined (*x’s*). There is a clear separation of the points, with disk hosts having low equivalent widths and luminosities and elliptical hosts having high equivalent widths and luminosities. This confirms the result found in Paper II that there are different types of object in the FIR-luminous radio-excess sample. Taken together, Figures 10 and 11 suggest that disk hosts have post-starburst type spectra, while elliptical hosts have an older stellar population or no stellar continuum. However, we do not find a clear relation between the continuum type and the host type. The stellar continuum type is probably more fundamentally related to the weakness of the ac-



tive nucleus. The objects that show strong stellar absorption also show more dominant starburst activity in their optical spectra. Figure 12 shows the diagnostic diagrams, with the same symbols as in Figure 10 showing the objects with A-star stellar continuum, older stellar continuum, and minimal stellar continuum in their spectra. The post-starburst objects tend to cluster around the maximum starburst and mixing lines and have ambiguous or borderline classifications. The objects with older stellar continuum or no stellar continuum tend to fall higher in the diagnostic diagrams, indicating a more dominant AGN.

Figure 13 shows the same equivalent width – luminosity diagram as Figures 10 and 11, with data for CSS sources from Gelderman & Whittle (1994) plotted for comparison. The FIR-luminous radio-excess and CSS samples follow the same trend of [O III]  $\lambda 5007$  equivalent width versus luminosity. We suggest that the four CSS objects in the lower left part of the diagram are likely to be post-starburst AGN. Examination of the spectra presented in Gelderman & Whittle (1994) supports this hypothesis: all of the four CSS sources with [O III]  $\lambda 5007$  luminosities less than  $10^{41.5}$  erg s<sup>-1</sup> show Mg b and Na D stellar absorption and two show H $\beta$  absorption, indicative of an intermediate-age stellar population.

#### 4.5. The Nature of Radio-Excess *IRAS* Galaxies

Radio-excess galaxies have been identified in small numbers by previous authors but, prior to this work, have not previously been studied as a class. Our multi-wavelength study has shown that these objects are more common than generally believed and that the radio excess is an excellent indicator of the presence of an active nucleus. Most of the FIR-luminous radio-excess objects have compact radio sources, as shown by our radio observations (Paper III). Sixty-five percent of the radio sources are less than 10 kpc in size and have radio sizes an order of magnitude smaller than the optical extent. The more extended objects are classical radio galaxies but the compact radio sources appear to be a different population of objects.

The compact FIR-luminous radio-excess galaxies have steep radio spectra indicative of optically thin synchrotron emission, but radio powers in be-

tween those of traditional Seyfert and CSS/GPS sources. Modeling of the radio data suggests that the radio sources have ages  $10^4 - 10^6$  years (Paper III), placing them among the young radio sources. Synchrotron and jet models used to interpret the radio and optical data show that the radio jets in the radio-excess galaxies are intrinsically less powerful than radio sources such as CSS/GPS sources. This suggests that the intrinsic jet energy flux is the dominant factor determining the weaker radio power in the radio-intermediate sources. We interpret the high ratios of [O III]  $\lambda 5007$  luminosity to radio power in the radio-excess objects to be a result of slower, more luminous shocks in the radio-excess sources than in more powerful radio sources. This is supported by the derived expansion velocities ( $< 0.01c$ ), which are significantly less than those observed in CSS/GPS sources. The FIR-luminous radio-excess objects also show evidence for strong interaction between the radio jet and the interstellar medium. Properties of the optical emission lines indicate the effect of the jet and expanding radio lobe on the kinematics of the line-emitting region. Two representative radio-excess sources observed with VLBI imaging, F11243-2244 and F23400-8705, have kiloparsec-scale lobes. Their morphologies are not similar to the symmetric doubles seen among the classes of CSS/GPS sources and suggest that the weaker radio jets are disrupted by interaction with the interstellar medium. The compact radio-excess sources are not likely to evolve into classical radio galaxies. Although we showed in Paper II that the host galaxies are more like those of FR II radio galaxies than FR Is, the radio powers are expected to decrease as the objects evolve, so that, if they were to expand to sizes of hundreds of kiloparsecs, the radio-excess objects would be unlikely to have FR II radio powers.

The radio-intermediate sources may be confined by the host interstellar medium; further work is required to determine if this is likely. An H I absorption study would allow us to estimate the gas masses in the radio-excess galaxies and determine if this is sufficient to confine the radio plasma.

The radio emission may be a transient phenomenon, perhaps associated with additional fueling to the black hole accretion disk in the nucleus. The FIR-luminous radio-excess objects may then fade to become radio-quiet galaxies. This would

be consistent with the large fraction of mergers in the sample. The optical morphologies of the host galaxies of the sample objects include a large fraction of merging or disturbed galaxies (Paper II). The post-starburst continuum spectra observed in one third of the sample provide further evidence that many of the hosts have undergone interactions. The dynamical timescale for merging activity and the age of the A-star population responsible for the post-starburst spectrum are both  $\sim 10^8$  years. The radio sources are at least two orders of magnitude younger than this. Therefore, if the radio activity is associated with the tidal interaction, then there must be a delay between the interaction and the initiation of radio activity.

There may be some influence of the host type on the radio power; radio sources with large radio excesses are not found in disk host galaxies (Paper II). Model-fitting of host surface brightness profiles suggests that there are two populations of host galaxy in the FIR-luminous radio-excess sample: disk and elliptical systems, with different host luminosities and radio excess distributions (Paper II). The disk systems have low radio excesses and host luminosities, while the elliptical hosts have a broad range of radio excesses and high optical luminosities. This result suggests that an elliptical host is necessary but not sufficient for a galaxy to host a radio-loud nucleus. However, the presence of both disk and elliptical galaxies together with the presence of objects in our sample that lie between radio-loud and radio-quiet objects in their radio/far-infrared and radio/[O III]  $\lambda 5007$  luminosity ratios shows that the classic dichotomy between radio-loud and radio-quiet galaxies, at the very least needs to be modified. The compact radio-intermediate objects that appear in our sample are AGN with relatively weak radio activity and a range of host morphologies, that fill the gap between powerful CSS/GPS sources and radio-quiet Seyfert galaxies.

## 5. Conclusions

Analysis of the optical spectra of our sample of FIR-luminous radio-excess galaxies confirms that radio-excess is an extraordinarily good indicator of the presence of an AGN. We find a much higher fraction of AGN than samples selected on FIR luminosity alone, or using other criteria such as

warm FIR colors. We find several ambiguous or borderline objects in the sample. These are likely to be composite objects that comprise starbursts which also host an AGN. There is some indication that the type of optical spectrum is associated with the radio-loudness, in that the radio-loud objects appear to be more ‘pure’ AGN than radio-intermediate objects. They may be more powerful AGN, though they still appear to be highly obscured.

In the [O III]  $\lambda 5007$  luminosity versus radio power diagram, the objects fall between the known correlations observed for radio galaxies and Seyferts. We interpret this in the context of shock models describing the interaction of the jet with the surrounding medium and infer that radio-intermediate objects generally have lower jet powers than more powerful radio sources. From our understanding that the jet powers of radio-excess objects are intrinsically lower than in CSS/GPS sources (Paper III), we infer that the radio-excess objects are equally luminous in [O III]  $\lambda 5007$  because the covering factor of dense gas is larger. This is supported by the lower expansion velocities inferred for the radio-excess objects (Paper III).

Despite the lower jet powers, the FIR-luminous radio-excess galaxies show clear evidence for strong interaction between the radio jet and the interstellar medium. Broad [O III]  $\lambda 5007$  line widths indicate acceleration of the line-emitting material by the radio source. A blueshift is observed between the [O III]  $\lambda 5007$  and  $H\alpha$  emission lines in several sources. Line profiles of two objects observed at higher spectral resolution show complex structure. These further suggest that the kinematics of the line-emitting material is strongly influenced by the radio source.

We find that 33% of the sample spectra show post-starburst stellar continuum, with A-star absorption lines. A further 13% show old, red stellar continuum and absorption typical of elliptical galaxies. The objects with post-starburst spectra appear to have weaker AGN; they have low [O III]  $\lambda 5007$  luminosities and equivalent widths, and lie closer to the starburst line in diagnostic diagrams. The objects with older stellar continuum show intermediate [O III]  $\lambda 5007$  luminosities and equivalent widths, and lie more clearly in the region of diagnostic diagrams occupied by Seyfert

galaxies. Objects with minimal stellar continuum have high luminosities and equivalent widths, and also occupy the Seyfert region of the diagnostic diagrams. The optical emission from these objects is clearly dominated by the active nucleus.

The presence of post-starburst AGN in the sample is consistent with the large number of merging or disturbed host galaxies found in the sample (Paper II). If the radio sources are associated with the merging activity, there must be a delay between the interaction and the initiation of the radio activity. The A-star spectra indicate ages of  $\sim 10^8$  years for the dominant stellar population, consistent with the dynamical timescales involved in mergers (Barnes & Hernquist 1996). The ages of the radio sources are likely to be at least two orders of magnitude younger than this.

Combining the understanding we have gleaned from our multi-wavelength study, we find that the radio-intermediate objects span a range of properties between those of powerful radio sources, such as CSS/GPS sources, and radio-quiet Seyfert galaxies. It remains unclear whether the radio-intermediate objects reveal a continuum of radio-loudness in AGN or indicate that the distributions of radio-loud and radio-quiet AGN overlap. The compact radio-intermediate objects in the FIR-luminous radio-excess sample appear to be a new population of relatively young radio sources that will not evolve into classical radio galaxies, but which are more powerful than typical radio-quiet Seyferts. Further observations are required to determine if the radio plasma is confined by the host interstellar medium.

CLB wishes to acknowledge the support of an Australian Postgraduate Research Award and a Duffield Scholarship. MAD wishes to acknowledge the support of the Australian National University and the Australian Research Council (ARC) through his ARC Australian Federation Fellowship, and also under ARC Discovery project DP0208445. GVB acknowledges support from the ARC Large Grant A699050341. We thank the referee for helpful comments which improved the manuscript.

## REFERENCES

Barnes, J. E., & Hernquist, L. 1996, *ApJ*, 471, 115  
 Baum, S. A., & Heckman, T. 1989, *ApJ*, 336, 702

Baum, S. A., & McCarthy, P. J. 2000, *AJ*, 119, 2634  
 Best, P. N., Inskip, K. J., Röttgering, H. J. A., & Longair, M. S. 2002, *Rev. Mexicana Astron. Astrofis.*, 13, 155  
 Best, P. N., Röttgering, H. J., & Longair, M. S. 1999, in *ASP Conf. Ser. 193, The Hy-Redshift Universe: Galaxy Formation and Evolution at High Redshift*, ed. A. J. Bunker, & W. J. M. van Breugel (San Francisco: ASP), 71  
 Best, P. N., Röttgering, H. J. A., & Longair, M. S. 2000, *MNRAS*, 311, 1  
 Bicknell, G. V., Dopita, M. A., & O’Dea, C. P. 1997, *ApJ*, 485, 112  
 Bicknell, G. V., Dopita, M. A., Tsvetanov, Z. I., & Sutherland, R. S. 1998, *ApJ*, 495, 680  
 Bicknell, G. V., Saxton, C. J., & Sutherland, R. S. 2003, *PASA*, 20, 102  
 Condon, J. J., Anderson, E., & Broderick, J. J. 1995, *AJ*, 109, 2318  
 Conway, J. E. 2002, *New A Rev.*, 46, 263  
 Corbett, E. A., Kewley, L. J., Appleton, P. N., Charmandaris, V., Dopita, M. A., Heisler, C. A., Norris, R. P., Zezas, A., & Marston, A. 2003, *ApJ*, 583, 670  
 de Bruyn, A. G., & Wilson, A. S. 1978, *A&A*, 64, 433  
 de Grijp, M. H. K., Keel, W. C., Miley, G. K., Goudfrooij, P., & Lub, J. 1992, *A&AS*, 96, 389  
 Dey, A., & van Breugel, W. 1994, in *Mass-Transfer Induced Activity in Galaxies*, ed. I. Shlosman (Cambridge: Cambridge University Press), 263  
 Dopita, M. A., Heisler, C. A., Lumsden, S., & Bailey, J. 1998, *ApJ*, 498, 570  
 Drake, C. L., Bicknell, G. V., McGregor, P. J., & Dopita, M. A. 2004b, *AJ*, 128, 969 Paper III  
 Drake, C. L., McGregor, P. J., & Dopita, M. A. 2004a, *AJ*, 128, 955 Paper II  
 Drake, C. L., McGregor, P. J., Dopita, M. A., & van Breugel, W. J. M. 2003, *AJ*, 126, 2237 Paper I  
 Edelson, R. A. 1987, *ApJ*, 313, 651  
 Gelderman, R., & Whittle, M. 1994, *ApJS*, 91, 491  
 Griffith, M. R., & Wright, A. E. 1993, *AJ*, 105, 1666  
 Griffith, M. R., Wright, A. E., Burke, B. F., & Ekers, R. D. 1994, *ApJS*, 90, 179  
 Griffith, M. R., Wright, A. E., Burke, B. F., & Ekers, R. D. 1995, *ApJS*, 97, 347  
 Holt, J., Tadhunter, C. N., & Morganti, R. 2003, *MNRAS*, 342, 227  
 Inskip, K. J., Best, P. N., Rawlings, S., Longair, M. S., Cotter, G., Röttgering, H. J. A., Eales, S. 2002a, *MNRAS*, 337, 1381  
 Inskip, K. J., Best, P. N., Röttgering, H. J. A., Rawlings, S., Cotter, G., & Longair, M. S. 2002b, *MNRAS*, 337, 1407  
 Kewley, L. J., Heisler, C. A., Dopita, M. A., & Lumsden, S. 2001, *ApJS*, 132, 37

- Koekemoer, A. M., & Bicknell, G. V. 1998, *ApJ*, 497, 662
- Koekemoer, A. M., & Bicknell, G. V. 2002, *New A Rev.*, 46, 197
- Kühr, H., Witzel, A., Pauliny-Toth, I. I. K., & Nauber, U. 1981, *A&AS*, 45, 367
- Miller, J. S., & Mathews, W. G. 1972, *ApJ*, 172, 593
- Moshir, M., et al. 1992, Explanatory Supplement to the *IRAS* Faint Source Survey, Version 2, JPL D-10015 8/92 (Pasadena: JPL)
- Murgia, M., Fanti, C., Fanti, R., Gregorini, L., Klein, U., Mack, K.-H., & Vigotti, M. 1999, *A&A*, 345, 769
- Murgia, M., Fanti, C., Fanti, R., Gregorini, L., Klein, U., Mack, K.-H., & Vigotti, M. 2002, *New A Rev.*, 46, 307
- Murgia, M. 2003, *PASA*, 20, 19
- O'Dea, C. P., de Vries, W. H., Koekemoer, A. M., Baum, S. A., Morganti, R., Fanti, R., Capetti, A., Tadhunter, C. N., Barthel, P. D., Axon, D. J., & Gelderman, R. 2002, *AJ*, 123, 2333
- O'Dea, C. P., de Vries, W. H., Koekemoer, A. M., Baum, S. A., Axon, D. J., Barthel, P. D., Capetti, A., Fanti, R., Gelderman, R., Morganti, R., & Tadhunter, C. N. 2003, *PASA*, 20, 88
- Owsianik, I., & Conway, J. E. 1998, *A&A*, 337, 69
- Owsianik, I., Conway, J. E., & Polatidis, A. G. 1999, *New A Rev.*, 43, 669
- Parma, P., Murgia, M., Morganti, R., Capetti, A., de Ruiter, H. R., & Fanti, R., 1999, *A&A*, 344, 7
- Rawlings, S., & Saunders, R. 1991, *Nature*, 349, 138
- Solórzano-Iñarrea, C., Tadhunter, C. N., & Axon, D. J. 2001, *MNRAS*, 323, 965
- Solórzano-Iñarrea, C., Tadhunter, C., & Bland-Hawthorn, J. 2002, *MNRAS*, 331, 673
- Tadhunter, C. N. 1991, *MNRAS*, 251, 46p
- Tadhunter, C. N., Morganti, R., di Serego-Alighieri, S., Fosbury, R. A. E., & Danziger, I. J. 1993, *MNRAS*, 263, 999
- Tadhunter, C. N., Morganti, R., Robinson, A., Dickson, R., Villar-Martin, M., & Fosbury, R. A. E. 1998, *MNRAS*, 298, 1035
- Tadhunter, C., Wills, K., Morganti, R., Oosterloo, T., & Dickson, R. 2001, *MNRAS*, 327, 227
- van Breugel, W., Heckman, T., Butcher, H., & Miley, G. 1984a, *ApJ*, 277, 82
- van Breugel, W., Heckman, T., & Miley, G. 1984b, *ApJ*, 276, 79
- Veilleux, S. 2002, in *ASP Conf. Ser.* 284, *AGN Surveys*, ed. R. F. Green, E. Ye. Khachikian, & D. B. Sanders (San Francisco: ASP), 111
- Veilleux, S., Kim, D.-C., & Sanders, D. B. 1999, *ApJ*, 522, 113
- Veilleux, S., Kim, D.-C., Sanders, D. B., Mazzarella, J. M. & Soifer, B. T. 1995, *ApJS*, 98, 171
- Veilleux, S., & Osterbrock, D. E. 1987, *ApJS*, 63, 295
- Veilleux, S., Sanders, D. B., & Kim, D.-C. 1997, *ApJ*, 484, 92
- Villar-Martín, M., Tadhunter, C., Morganti, R., Axon, D., & Koekemoer, A. 1999, *MNRAS*, 307, 24
- Wall, J. V., & Peacock, J. A. 1985, *MNRAS*, 216, 173
- Whittle, M. 1992a, *ApJS*, 79, 49
- Whittle, M. 1992b, *ApJS*, 387, 109
- Whittle, M. 1985, *MNRAS*, 213, 33
- Wilson, A. S., & Colbert, E. J. M. 1995, *ApJ*, 438, 62
- Wright, A. E., Griffith, M. R., Burke, B. F., & Ekers, R. D. 1994, *ApJS*, 91, 111
- Wright, A. E., Griffith, M. R., Hunt, A. J., Troup, E., Burke, B. F., & Ekers, R. D. 1996, *ApJS*, 103, 145

---

This 2-column preprint was prepared with the AAS L<sup>A</sup>T<sub>E</sub>X macros v5.2.

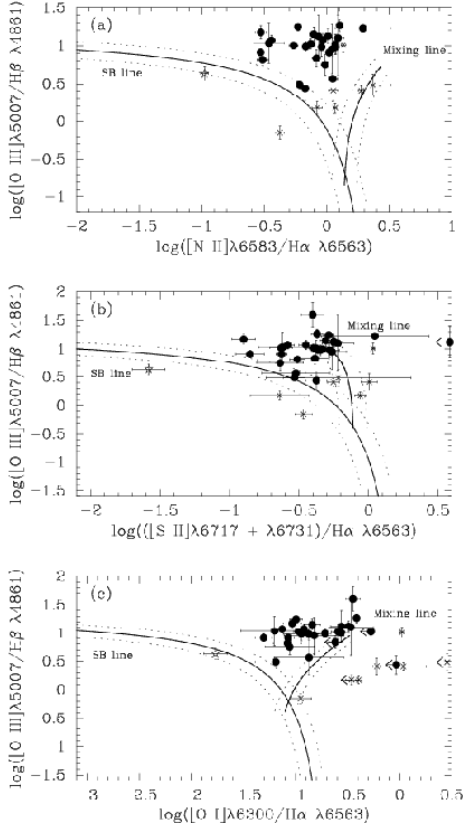


Fig. 1.— Diagnostic diagrams. (a)  $\log([\text{O III}] \lambda 5007/\text{H}\beta \lambda 4861)$  vs  $\log([\text{N II}] \lambda 6584/\text{H}\alpha)$ . (b)  $\log([\text{O III}] \lambda 5007/\text{H}\beta \lambda 4861)$  vs  $\log(([\text{S II}] \lambda 6717 + [\text{S II}] \lambda 6731)/\text{H}\alpha)$ . (c)  $\log([\text{O III}] \lambda 5007/\text{H}\beta \lambda 4861)$  vs  $\log([\text{O I}] \lambda 6300/\text{H}\alpha)$ . Seyfert galaxies (*filled circles*), LINERs (*open squares*), and starburst galaxies (*open stars*) are classified according to their location relative to the maximum starburst line (*solid line*) and extreme mixing line (*solid line*) (Kewley et al. 2001). Objects are classified as ambiguous (*x's*) if they fall in different regions in different diagrams. Line fluxes have been corrected for reddening.

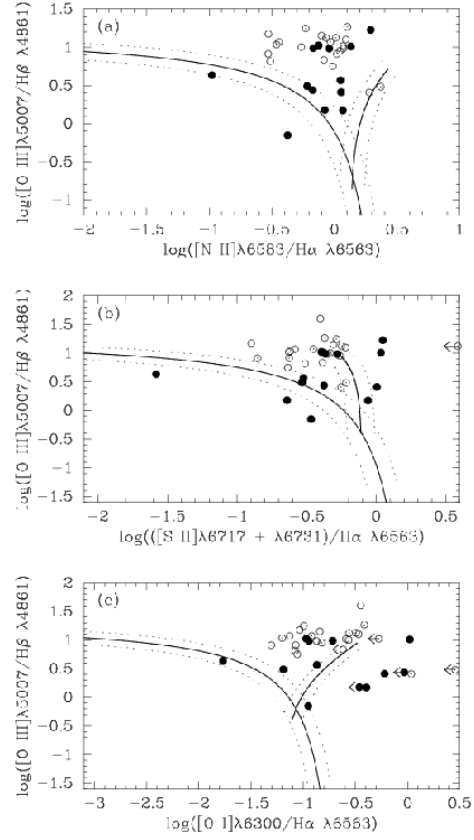


Fig. 2.— Diagnostic diagrams. The symbols indicate the level of radio excess, radio-loud (*open circles*) or radio-intermediate (*filled circles*).

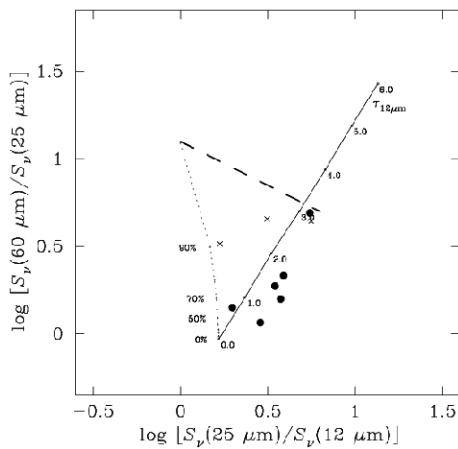


Fig. 3.— FIR color-color diagram for objects with measured *IRAS* 25  $\mu\text{m}$  and 12  $\mu\text{m}$  fluxes. The symbols indicate the classification assigned to the objects based on the diagnostic diagrams, Seyfert (*filled circles*) or ambiguous (*x's*). The loci marked on the diagram follow Dopita et al. (1998). The solid line is a reddening line produced by increasing the optical depth,  $\tau_{12\mu\text{m}}$ , through which a pure Seyfert nucleus is observed. The dotted line is a mixing line indicating the location of objects comprising a mixture of pure AGN (0% starburst) and increasing fractions of starburst. The dashed line indicates the location of starburst galaxies.

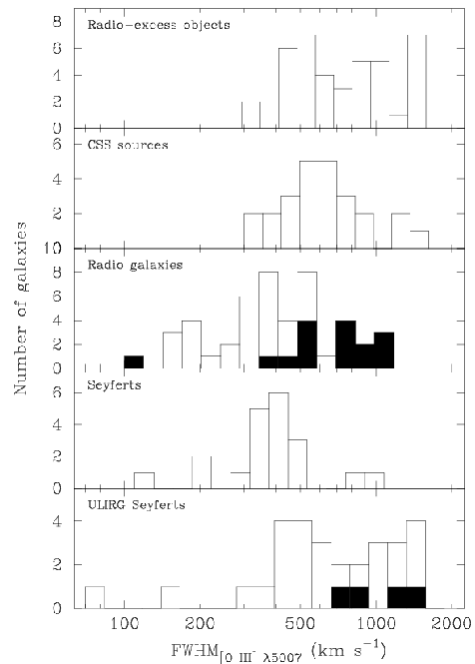


Fig. 4.— The distribution of [O III]  $\lambda 5007$  emission line widths for the FIR-luminous radio-excess sample and comparison objects. CSS sources are from Gelderman & Whittle (1994), radio-galaxies from Baum & McCarthy (2000), Seyfert galaxies with linear radio sources are from Whittle (1992a), and ULIRG Seyferts are from Veilleux, Kim, & Sanders (1999). Filled regions are explained in the text.

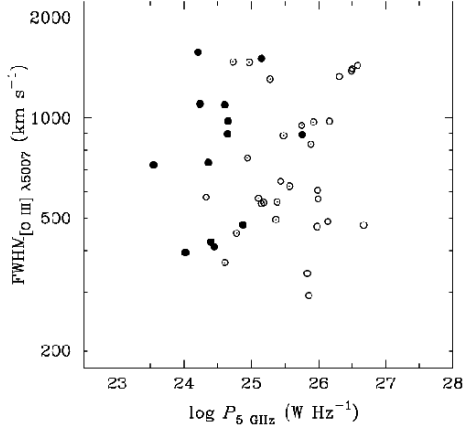


Fig. 5.— The [O III]  $\lambda 5007$  emission line width relative to the radio power. The symbols indicate the level of radio excess:  $u < 0.0$  (radio-loud; *open circles*),  $0.0 < u < 1.0$  (*dotted circles*), and  $1.0 < u < 1.8$  (*filled circles*). We note that the apparent correlation between the radio power and radio excess is a selection effect in our sample.

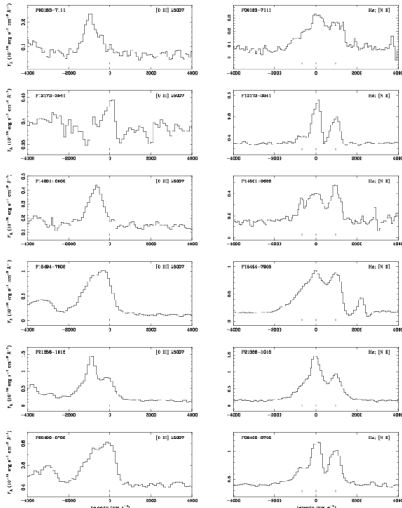


Fig. 6.— Plots of the spectra of six objects showing a blueshift between the [O III]  $\lambda 5007$  and  $H\alpha$  emission lines. Each line shows one object, with the left and right panels showing the [O III]  $\lambda 5007$  and  $H\alpha$  lines, respectively. The vertical scale is in units of  $10^{-15}$   $\text{erg s}^{-1} \text{cm}^{-2} \text{\AA}^{-1}$ , and the horizontal scale in units of  $\text{km s}^{-1}$ .

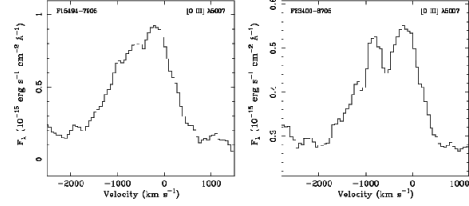


Fig. 7.— Plots of the [O III]  $\lambda 5007$  line profiles of two objects observed at higher resolution, showing the complex structure. The vertical scale is in units of  $10^{-15}$   $\text{erg s}^{-1} \text{cm}^{-2} \text{\AA}^{-1}$ , and the horizontal scale in units of  $\text{km s}^{-1}$ .

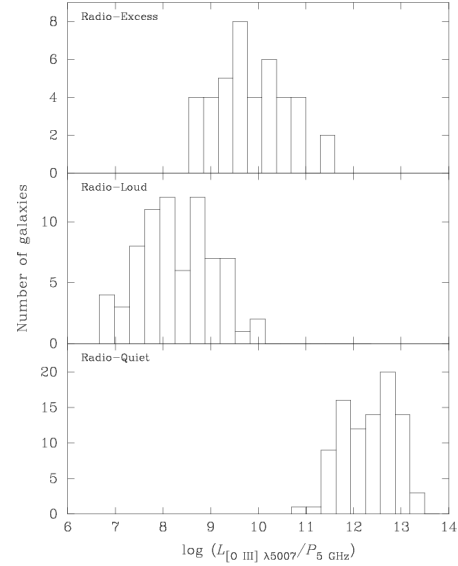


Fig. 8.— The distribution of the ratio of [O III]  $\lambda 5007$  luminosity to radio power for the radio-excess sample (*top panel*), for powerful radio sources (*middle panel*), and for radio-quiet Seyfert galaxies (*bottom panel*). The radio-loud objects include radio galaxies from Condon et al. (1995); Tadhunter et al. (1993); Wall & Peacock (1985); Kühr et al. (1981) and CSS sources from Gelderman & Whittle (1994). The data for the radio-quiet galaxies are from Condon et al. (1995); Whittle (1992a); Edelson (1987).

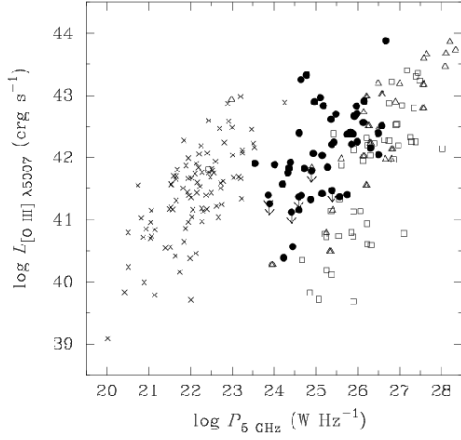


Fig. 9.— The [O III]  $\lambda 5007$  emission line luminosity relative to the radio power for the FIR-luminous radio-excess sample objects (*filled circles*). The comparison objects comprise Seyfert galaxies (*x's*), radio galaxies (*open squares*), and CSS sources (*open triangles*). References for the comparison objects are given in Figure 8.

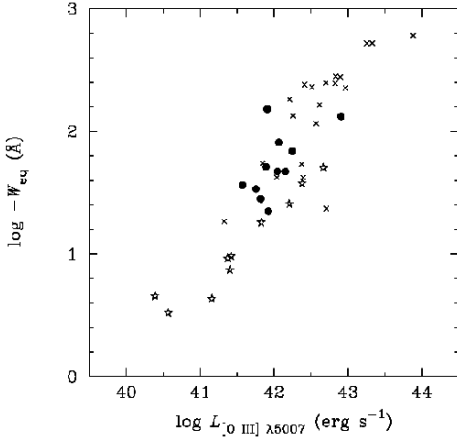


Fig. 10.— [O III]  $\lambda 5007$  equivalent widths versus [O III]  $\lambda 5007$  luminosity as a function of classification by stellar continuum type. The symbols indicate the type of stellar continuum in the spectrum; A-star spectra (*open stars*), older stellar continuum, typical of elliptical galaxies (*filled circles*), and objects with minimal stellar continuum (*x's*).

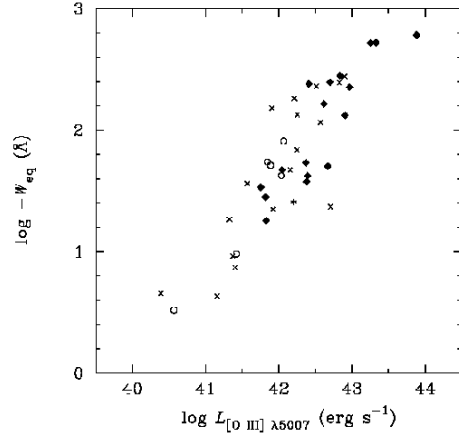


Fig. 11.— [O III]  $\lambda 5007$  equivalent widths versus [O III]  $\lambda 5007$  luminosity as a function of morphological type for the FIR-luminous radio-excess sample. Symbols indicate the host morphology, either disk (*open circles*), elliptical (*filled squares*), point source (*stars*), or undetermined (*x's*).



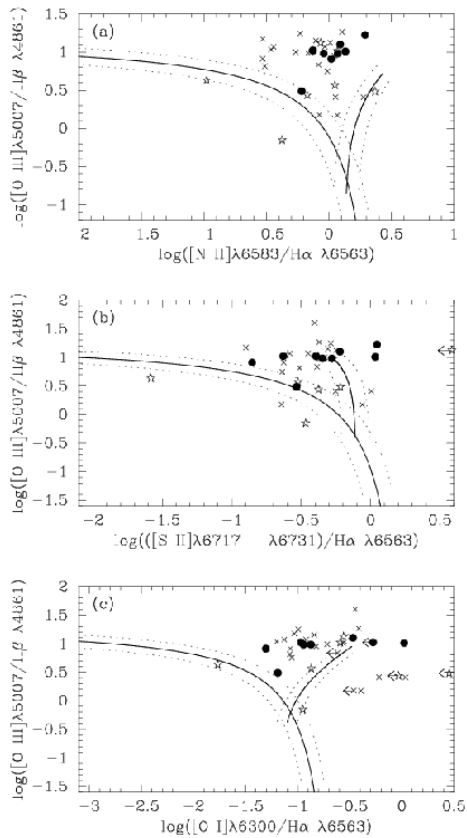


Fig. 12.— Diagnostic diagrams. The symbols indicate the presence of a dominant post-starburst population (*open stars*), old stellar population (*filled circles*), or no stellar absorption in the spectrum (*x's*).

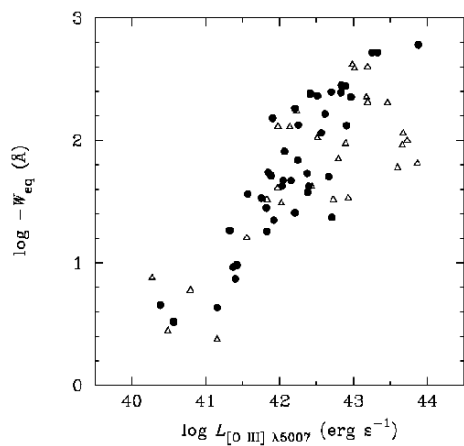


Fig. 13.—  $[\text{O III}] \lambda 5007$  equivalent widths versus  $[\text{O III}] \lambda 5007$  equivalent widths for the FIR-luminous radio-excess sample (*filled circles*) and CSS sources (*open triangles*; Gelderman & Whittle 1994).

TABLE 1  
 $H\alpha$  AND  $H\beta$  FLUXES AND EXTINCTION.

FSC Name	$z$	$H\alpha$ Flux <sup>a</sup>		$H\beta$ Flux <sup>a</sup>		E(B-V)
		narrow	broad	narrow	broad	
F00022+1231	0.143	15.80 ± 0.4	...	4.11 ± 0.2	...	0.2
F00183-7111	0.327	5.11 ± 0.3	...	1.74 ± 0.6	...	> 0.0
F01009-3241	0.256	13.80 ± 0.3	...	0.70 ± 0.1	...	1.8
F01477-1655	0.162	54.50 ± 1.5	...	16.04 ± 1.0	...	0.1
F02483-5456	0.394	3.57 ± 0.2	...	0.40 ± 0.2	...	1.1
F03169+1850	0.300	1.41 ± 0.1	...	< 0.94	...	> 0.0
F03265-2852	0.108	29.10 ± 0.9	...	8.61 ± 0.7	...	0.1
F04137-1144	0.090	3.93 ± 0.8	...	< 6.73	...	> 0.0
F04367-2726	0.111	27.40 ± 0.7	...	4.51 ± 0.5	...	0.7
F05246+0103	0.097	17.10 ± 0.8	...	3.12 ± 0.6	...	0.6
F05265-4720	0.134	3.88 ± 0.3	...	< 3.92	...	> 0.0
F06065-7934	0.287	4.97 ± 1.3	...	< 0.93	...	> 0.5
F06195-4503	0.206	7.38 ± 0.3	...	1.22 ± 0.2	...	0.7
F08064-1018	0.110	39.50 ± 0.8	...	10.22 ± 0.4	...	0.2
F09165-0726	0.273	1.09 ± 0.1	...	< 1.32	...	> 0.0
F09323+0732	0.290	5.30 ± 0.2	...	1.55 ± 0.2	...	0.1
F09416-0137	0.112	11.70 ± 0.8	...	0.55 ± 0.5	...	1.9
F10227-8251	0.086	11.40 ± 0.4	...	2.30 ± 0.3	...	0.5
F10418+1153	0.230	2.69 ± 0.1	...	< 1.97	...	> 0.0
F11243-2244	0.171	12.20 ± 0.2	20.80 ± 0.5	0.89 ± 0.1	0.64 ± 0.4	1.5
F11270+0031	0.211	2.34 ± 0.1	...	0.77 ± 0.1	...	> 0.0
F12173-3541	0.057	5.93 ± 0.2	...	0.54 ± 0.1	...	1.3
F12183-1015	0.300	0.91 ± 0.1	...	< 0.51	...	> 0.0
F14381-3901	0.138	43.10 ± 0.8	26.20 ± 4.4	9.14 ± 0.4	5.18 ± 3.2	0.4
F14501+0639	0.267	6.13 ± 0.3	...	< 4.12	...	> 0.0
F15129+0432	0.095	7.13 ± 0.2	...	1.20 ± 0.1	...	0.7
F15494-7905	0.150	9.07 ± 0.3	15.30 ± 1.0	0.66 ± 0.2	2.01 ± 0.8	1.5
F15599+0206	0.104	20.90 ± 0.5	...	5.18 ± 0.3	...	0.3
F16159-0402	0.213	21.70 ± 0.4	...	3.11 ± 0.4	...	0.8
F16431+0217	0.096	20.90 ± 0.6	...	4.21 ± 0.5	...	0.5
F17345+1124	0.165	56.60 ± 0.9	...	14.21 ± 0.6	...	0.3
F19254-7245	0.062	18.40 ± 0.5	130.00 ± 2.0	1.88 ± 0.3	1.37 ± 1.5	1.2
F20203-5733	0.352	29.70 ± 0.5	120.00 ± 3.0	8.12 ± 0.3	10.60 ± 2.2	0.2
F20517-5809	0.193	4.53 ± 0.4	...	< 2.85	...	> 0.0
F21139-6613	0.153	71.50 ± 1.2	...	1.02 ± 0.3	...	3.1
F21309-0726	0.087	12.00 ± 0.3	...	1.42 ± 0.2	...	1.0
F21356-1015	0.206	18.50 ± 0.4	17.70 ± 1.0	1.97 ± 0.2	1.35 ± 0.7	1.1
F21497-0824	0.035	73.80 ± 1.2	...	13.45 ± 0.6	...	0.6
F21511-4606	0.146	9.67 ± 0.3	14.10 ± 2.6	1.79 ± 0.2	2.38 ± 1.9	0.6
F21527-2856	0.232	< 1.95	...	< 0.94	...	...
F22537-6512	0.120	45.80 ± 1.0	...	11.65 ± 0.6	...	0.2
F23002-5828	0.210	26.50 ± 1.5	...	< 11.11	...	> 0.0
F23075-5957	0.141	1.48 ± 0.4	...	0.95 ± 0.3	...	> 0.0
F23140+0348	0.220	12.90 ± 0.4	...	0.86 ± 0.2	...	1.6
F23389+0300	0.145	15.10 ± 0.3	...	2.63 ± 0.3	...	0.6
F23400-8705	0.106	12.10 ± 0.4	...	< 7.18	...	> 0.0
F23475-7407	0.105	< 6.02	...	< 4.78	...	...
F23493-0126	0.174	25.40 ± 1.1	327.00 ± 9.7	6.24 ± 0.8	71.10 ± 7.1	0.3
F23565-7631	0.082	0.93 ± 0.4	...	0.36 ± 0.3	...	> 0.0

<sup>a</sup>Fluxes are in units of  $10^{-15}$  erg s<sup>-1</sup> cm<sup>-2</sup>.  
 $H\alpha$  and  $H\beta$  fluxes have not been corrected for reddening.

TABLE 2  
EMISSION LINE FLUXES.

FSC Name	[Ne V] λ3426	[O II] λ3727	[Ne III] λ3869	[O III] λ4363	He II λ4686	[O III] λ4959	[O III] λ5007	[O I] λ6300	[N II] λ6548	[N II] λ6584	[S II] λ6717	[S II] λ6731
F00022+1231	4.72	15.99	5.10	1.08	2.02	17.14	51.06	2.03	2.53	7.44	3.11	4.35
F00183-7111	< 1.18	6.85	1.73	< 1.48	< 1.49	1.62	4.49	3.08	1.93	5.77	3.19	1.98
F01009-3241	703.98	4763.	1267.	< 511.11	< 323.88	873.13	3262.	211.35	271.00	695.68	109.18	124.70
F01477-1655	16.22	41.94	18.22	3.62	5.49	77.52	228.76	4.12	7.69	22.57	8.78	7.03
F02483-5456	< 106.25	119.89	< 82.46	< 53.68	< 44.55	36.95	125.51	8.11	8.72	25.24	< 56.84	< 56.48
F03169+1850	< 0.33	0.73	0.53	< 0.52	0.33	< 2.26	2.54	< 2.10	0.91	2.92	0.41	0.08
F03265-2852	19.14	25.69	11.15	< 7.22	5.70	35.52	100.10	5.22	13.08	38.24	11.10	7.83
F04137-1144	< 2.15	0.83	< 1.25	< 1.16	< 1.23	< 3.82	< 3.64	< 4.38	0.76	2.24	0.80	0.69
F04367-2726	20.75	110.59	< 74.33	< 58.76	< 38.08	42.13	104.34	6.77	21.84	63.55	17.40	13.36
F05246+0103	< 38.67	< 35.00	49.74	< 28.12	< 22.38	< 31.88	25.98	< 18.48	15.38	44.80	8.22	4.02
F05265-4720	< 1.41	4.20	1.44	< 2.00	< 2.24	< 2.86	< 2.86	< 2.90	1.53	4.50	1.22	0.56
F06065-7934	< 4.40	10.18	6.86	< 5.07	< 4.66	6.53	16.95	< 4.49	5.30	15.48	0.29	4.97
F06195-4503	12.09	25.66	22.68	< 10.24	< 11.93	19.45	62.04	< 6.77	7.96	23.21	6.89	4.68
F08064-1018	26.75	40.28	20.71	4.97	7.98	76.02	232.52	4.56	7.57	22.15	9.48	6.55
F09165-0726	< 0.66	1.09	< 0.81	< 1.12	< 1.02	0.52	0.70	< 1.54	0.32	0.93	0.38	0.35
F09323+0732	1.07	7.08	3.17	< 2.51	< 2.12	7.52	26.28	2.20	2.71	7.95	2.14	1.74
F09416-0137	< 7219.	6818.	13400.	723.02	< 2167.	447.74	644.93	73.23	223.86	606.02	86.26	76.79
F10227-8251	< 26.64	52.81	14.61	< 21.82	< 21.96	32.69	90.10	3.30	9.04	26.37	8.25	7.02
F10418+1153	< 1.06	3.05	1.99	0.59	< 1.64	2.62	6.41	0.47	0.97	3.19	0.76	0.61
F11243-2244	449.08	544.20	166.28	< 169.48	15.57	186.32	626.47	11.79	86.09	248.39	15.49	17.90
F11270+0031	0.84	2.49	0.89	0.30	0.28	2.65	7.74	0.64	0.43	1.27	0.62	0.47
F12173-3541	< 929.58	416.77	< 428.82	23.67	< 198.12	42.48	65.99	< 69.23	17.36	50.09	22.45	9.03
F12183-1015	< 0.31	1.01	< 0.37	< 0.42	0.38	< 0.66	< 0.68	0.24	0.24	0.72	0.27	0.17
F14381-3901	< 15.53	103.49	29.89	12.64	3.50	87.52	262.43	8.45	10.05	29.45	14.65	8.94
F14501+0639	< 0.73	1.62	0.75	< 1.73	< 1.89	1.55	6.97	1.11	1.56	4.60	0.46	1.42
F15129+0432	< 52.36	48.62	< 42.56	2.05	< 23.21	2.84	5.95	2.92	3.79	11.03	5.58	3.32
F15494-7905	< 771.10	1068.	538.72	< 258.17	< 215.70	925.16	2271.	62.59	75.23	216.39	39.80	30.02
F15599+0206	24.10	31.21	13.95	6.59	5.26	54.16	161.66	5.11	9.50	27.88	10.92	6.53
F16159-0402	< 51.40	288.32	35.13	< 33.07	< 32.20	21.74	52.83	44.38	44.08	128.18	13.06	82.66
F16431+0217	24.42	42.67	14.20	12.66	8.37	54.23	165.90	7.18	21.60	62.99	12.37	11.74
F17345+1124	7.68	77.84	23.09	22.08	8.11	99.00	292.63	17.91	21.63	63.32	20.59	19.59
F19254-7245	< 975.59	963.08	< 478.67	< 383.22	< 287.96	251.71	602.16	192.02	85.52	247.36	103.95	93.19
F20203-5733	13.31	29.71	16.05	4.13	3.41	65.30	198.66	3.84	4.18	12.27	2.94	2.28
F20517-5809	< 1.89	2.45	< 1.94	< 2.52	1.67	< 3.49	< 3.49	0.58	1.17	3.45	0.80	1.04
F21139-6613	<695400.	583700.	92600.	16400.	<78500.	21900.	50000.	615.32	1353.	3796.	505.94	440.09
F21309-0726	203.05	158.70	88.64	< 112.09	29.65	115.27	299.30	< 46.76	22.58	65.48	12.47	8.29
F21356-1015	< 215.96	752.80	184.77	24.91	< 78.89	374.18	960.54	17.09	34.40	99.46	87.49	0.26
F21497-0824	< 102.02	194.04	94.31	20.42	26.21	265.04	783.17	24.66	58.92	172.12	49.04	44.07
F21511-4606	25.95	82.71	26.73	11.58	3.23	47.10	125.63	9.42	10.31	30.02	8.97	7.54
F21527-2856	...	...	...	...	...	...	...	...	...	...	...	...
F22537-6512	41.74	75.74	34.18	4.71	13.37	96.19	280.10	8.89	23.34	68.32	13.51	12.59
F23002-5828	< 3.21	4.96	< 3.67	< 3.46	< 3.22	< 4.86	1.18	< 5.84	0.36	1.06	1.59	0.59
F23075-5957	< 3.48	1.93	< 4.53	< 4.27	< 4.85	2.29	2.89	< 4.21	1.18	3.46	0.52	0.38
F23140+0348	549.98	5150.	363.80	< 853.04	< 612.95	480.54	997.58	76.25	121.01	347.55	64.23	60.54

TABLE 2—*Continued*

FSC Name	[Ne V] $\lambda 3426$	[O II] $\lambda 3727$	[Ne III] $\lambda 3869$	[O III] $\lambda 4363$	He II $\lambda 4686$	[O III] $\lambda 4959$	[O III] $\lambda 5007$	[O I] $\lambda 6300$	[N II] $\lambda 6548$	[N II] $\lambda 6584$	[S II] $\lambda 6717$	[S II] $\lambda 6731$
F23389+0300	< 21.91	109.67	8.55	< 18.01	< 14.28	19.72	42.62	55.90	33.43	97.38	15.57	13.22
F23400-8705	< 2.96	3.31	< 3.84	< 3.85	< 4.28	4.88	13.05	1.26	3.35	9.86	2.75	2.04
F23475-7407	...	...	...	...	...	...	...	...	...	...	...	...
F23493-0126	11.50	30.58	11.32	43.38	< 42.89	26.52	79.56	3.84	14.51	42.43	5.06	5.07
F23565-7631	< 2.50	1.45	< 2.66	< 3.60	< 3.92	< 6.19	< 5.99	< 6.70	0.62	1.81	0.29	0.74

NOTE.—Fluxes are in units of  $10^{-15}$  erg s $^{-1}$  cm $^{-2}$ .  
All fluxes have been corrected for reddening, listed in Table 1.

TABLE 3  
EMISSION LINE WIDTHS.

FSC Name	[Ne V]	[O II]	[Ne III]	[O III]	He II	H $\beta$		[O III]	[O III]	[O I]	H $\alpha$		[N II]	[N II]	[S II]	[S II]
	$\lambda$ 3426	$\lambda$ 3727	$\lambda$ 3869	$\lambda$ 4363	$\lambda$ 4686	narrow	broad	$\lambda$ 4959	$\lambda$ 5007	$\lambda$ 6300	narrow	broad	$\lambda$ 6548	$\lambda$ 6584	$\lambda$ 6717	$\lambda$ 6731
F00022+1231	279	395	522	364	266	439	...	343	342	720	476	...	376	374	403	651
F00183-7111	...	871	1375	...	...	2272	...	795	893	563	720	...	950	944	942	940
F01009-3241	419	688	725	...	...	511	...	633	887	599	770	...	769	679	683	681
F01477-1655	419	513	408	588	439	542	...	443	451	329	573	...	459	457	422	366
F02483-5456	...	751	...	...	...	762	...	914	974	323	691	...	693	689	...	...
F03169+1850	...	327	1107	...	187	...	...	...	1408	...	635	...	979	1063	1030	1027
F03265-2852	818	419	563	...	572	506	...	542	496	555	467	...	516	513	455	412
F04137-1144	...	606	...	...	...	...	...	...	...	...	1642	...	430	428	471	335
F04367-2726	590	372	...	...	...	500	...	513	425	624	506	...	532	529	558	557
F05246+0103	...	...	1040	...	...	207	...	...	479	...	175	...	471	468	262	214
F05265-4720	...	484	775	...	...	...	...	...	...	...	678	...	364	362	366	366
F06065-7934	...	481	780	...	...	...	...	1671	1335	...	506	...	638	634	1058	1055
F06195-4503	516	592	1061	...	...	406	...	256	573	...	514	...	515	512	469	468
F08064-1018	435	452	482	728	381	486	...	467	472	511	459	...	482	479	452	422
F09165-0726	...	538	...	...	...	...	...	723	951	...	572	...	523	521	1030	1028
F09323+0732	663	515	768	...	...	827	...	731	978	697	493	...	756	752	470	381
F09416-0137	...	460	2377	1027	...	384	...	1478	1095	510	524	...	599	559	529	528
F10227-8251	...	605	662	...	...	429	...	427	395	415	399	...	398	396	366	418
F10418+1153	...	505	807	681	...	...	...	836	560	155	216	...	225	296	249	249
F11243-2244	1590	563	348	...	164	664	2439	688	759	304	695	2448	697	693	698	697
F11270+0031	590	517	518	72	356	382	...	358	293	532	471	...	320	319	325	325
F12173-3541	...	511	...	613	...	480	...	1826	1104	...	355	...	399	397	532	272
F12183-1015	...	528	...	...	184	...	...	...	...	116	372	...	394	392	384	384
F14381-3901	...	598	572	1217	376	656	7234	556	558	568	482	7238	481	478	538	364
F14501+0639	...	570	1108	...	...	...	...	623	836	810	790	...	432	430	691	690
F15129+0432	...	511	...	526	...	275	...	117	411	326	204	...	259	257	260	218
F15494-7905	...	649	1025	...	...	665	2297	1676	1439	974	696	2306	697	693	458	577
F15599+0206	511	562	516	888	599	575	...	504	489	493	484	...	488	486	542	388
F16159-0402	...	1016	872	...	...	1335	...	1572	1510	915	771	...	779	775	1223	1221
F16431+0217	633	615	431	1329	802	693	...	642	646	605	514	...	622	618	648	646
F17345+1124	412	918	709	3195	1387	1025	...	922	897	1002	873	...	772	767	808	807
F19254-7245	...	812	...	...	...	459	2565	1823	1578	1650	524	2578	525	522	562	561
F20203-5733	453	608	493	575	674	718	8079	576	477	708	628	8084	630	626	374	373
F20517-5809	...	973	...	...	447	...	...	...	...	164	627	...	859	855	356	411
F21139-6613	...	735	516	412	...	609	...	508	735	369	482	...	461	459	432	399
F21309-0726	493	340	680	...	709	336	...	737	579	...	399	...	368	366	375	255
F21356-1015	...	759	882	584	...	505	2701	1455	1470	585	570	2714	571	568	1254	1304
F21497-0824	...	589	722	776	760	655	...	731	723	698	594	...	582	579	481	505
F21511-4606	471	455	429	444	284	357	4969	432	368	387	472	4974	577	574	392	294
F21527-2856	...	716	...	...	...	...	...	...	625	...	...	...	...	...	...	...
F22537-6512	658	606	655	672	617	617	...	593	575	515	440	...	516	514	397	397
F23002-5828	...	711	...	...	...	...	...	...	979	...	1955	...	677	673	678	677
F23075-5957	...	814	...	...	...	388	...	101	554	...	567	...	459	456	315	282
F23140+0348	449	1018	484	...	...	721	...	1399	1386	897	769	...	770	766	453	452

TABLE 3—*Continued*

FSC Name	[Ne V]	[O II]	[Ne III]	[O III]	He II	H $\beta$		[O III]	[O III]	[O I]	H $\alpha$		[N II]	[N II]	[S II]	[S II]
	$\lambda 3426$	$\lambda 3727$	$\lambda 3869$	$\lambda 4363$	$\lambda 4686$	narrow	broad	$\lambda 4959$	$\lambda 5007$	$\lambda 6300$	narrow	broad	$\lambda 6548$	$\lambda 6584$	$\lambda 6717$	$\lambda 6731$
F23389+0300	...	803	549	...	...	1137	...	1864	1308	1988	729	...	1181	1174	517	516
F23400-8705	...	406	...	...	...	...	...	1356	1476	803	558	...	525	523	562	561
F23475-7407	...	...	...	...	...	...	...	...	...	...	...	...	...	...	...	...
F23493-0126	567	724	770	4501	...	602	6563	639	607	459	622	6571	624	621	348	347
F23565-7631	...	425	...	...	...	571	...	...	...	...	629	...	466	463	341	340

NOTE.—All linewidths are in  $\text{km s}^{-1}$ .

TABLE 4  
[O III]  $\lambda 5007$  EQUIVALENT WIDTHS.

FSC Name	$W_{\text{eq}}$ (Å)	FSC Name	$W_{\text{eq}}$ (Å)
F00022+1231	-241.70	F15129+0432	-3.32
F00183-7111	-54.11	F15494-7905	-231.60
F01009-3241	-250.20	F15599+0206	-116.00
F01477-1655	-526.20	F16159-0402	-42.42
F02483-5456	-50.71	F16431+0217	-69.19
F03169+1850	-47.41	F17345+1124	-524.30
F03265-2852	-165.20	F19254-7245	-36.60
F04137-1144	-9.64	F20203-5733	-607.80
F04367-2726	-22.42	F20517-5809	...
F05246+0103	-18.54	F21139-6613	-18.13
F05265-4720	-4.71	F21309-0726	-34.06
F06065-7934	-47.27	F21356-1015	-278.90
F06195-4503	-134.70	F21497-0824	-152.60
F08064-1018	-247.50	F21511-4606	-42.28
F09165-0726	-7.46	F21527-2856	-9.25
F09323+0732	-133.30	F22537-6512	-226.50
F09416-0137	-4.32	F23002-5828	...
F10227-8251	-51.60	F23075-5957	-9.64
F10418+1153	-25.80	F23140+0348	...
F11243-2244	-81.47	F23389+0300	-55.05
F11270+0031	-183.40	F23400-8705	-28.28
F12173-3541	-4.55	F23475-7407	-0.84
F12183-1015	-3.34	F23493-0126	-23.60
F14381-3901	-282.00	F23565-7631	-1.51
F14501+0639	-37.89		

TABLE 5  
OBJECT CLASSIFICATIONS.

FSC Name	Individual classifications			Type
	[N II]/H $\alpha$	[S II]/H $\alpha$	[O I]/H $\alpha$	
F00022+1231	Sy	Sy	Sy	Sy
F00183-7111	Sy	Sy	LN	AMB
F01009-3241	Sy	Sy	Sy	Sy
F01477-1655	Sy	Sy	Sy	Sy
F02483-5456	Sy	(Sy)	Sy	Sy
F03169+1850	...	...	...	...
F03265-2852	Sy	Sy	Sy	Sy
F04137-1144	...	...	...	...
F04367-2726	Sy	Sy	Sy	Sy
F05246+0103	Sy	SB	(LN)	AMB
F05265-4720	...	...	...	...
F06065-7934	...	...	...	...
F06195-4503	Sy	Sy	(Sy)	Sy
F08064-1018	Sy	Sy	Sy	Sy
F09165-0726	...	...	...	...
F09323+0732	Sy	Sy	Sy	Sy
F09416-0137	Sy	Sy	Sy	Sy
F10227-8251	Sy	Sy	Sy	Sy
F10418+1153	...	...	...	...
F11243-2244	Sy	Sy	Sy	Sy
F11270+0031	Sy	Sy	Sy	Sy
F12173-3541	Sy	Sy	(LN)	Sy
F12183-1015	...	...	...	...
F14381-3901	Sy	Sy	Sy	Sy
F14501+0639	...	...	...	...
F15129+0432	SB	SB	LN	AMB
F15494-7905	Sy	Sy	Sy	Sy
F15599+0206	Sy	Sy	Sy	Sy
F16159-0402	Sy	Sy	LN	AMB
F16431+0217	Sy	Sy	Sy	Sy
F17345+1124	Sy	Sy	Sy	Sy
F19254-7245	Sy	Sy	LN	AMB
F20203-5733	Sy	Sy	Sy	Sy
F20517-5809	...	...	...	...
F21139-6613	SB	SB	SB	SB
F21309-0726	Sy	Sy	(LN)	Sy
F21356-1015	Sy	Sy	Sy	Sy
F21497-0824	Sy	Sy	Sy	Sy
F21511-4606	Sy	Sy	Sy	Sy
F21527-2856	...	...	...	...
F22537-6512	Sy	Sy	Sy	Sy
F23002-5828	...	...	...	...
F23075-5957	LN	Sy	(LN)	AMB
F23140+0348	Sy	Sy	Sy	Sy
F23389+0300	Sy	Sy	LN	AMB
F23400-8705	...	...	...	...
F23475-7407	...	...	...	...
F23493-0126	Sy	Sy	Sy	Sy
F23565-7631	(Sy)	(Sy)	(LN)	Sy

NOTE.—Parentheses indicate a classification made using a limit in the line ratio; these were not used in assigning the final type. Objects for which H $\alpha$  or H $\beta$  is a limit were not classified.



TABLE 6  
JET ENERGY FLUXES.

FSC Name	$u$	$\log L_{[\text{O III}]}$ (W)	$\log P_{5 \text{ GHz}}$ (W Hz $^{-1}$ )	$\log F_E$ (W)
F00022+1231	-0.18	35.41	25.83	37.45
F00183-7111	1.04	35.37	25.76	37.41
F01009-3241	0.48	35.70	25.48	37.74
F01477-1655	0.74	36.33	24.78	38.36
F02483-5456	0.20	35.67	25.93	37.70
F03169+1850	-0.45	35.05	26.50	37.08
F03265-2852	0.03	35.61	25.36	37.65
F04137-1144	0.86	< 34.12	24.42	< 36.16
F04367-2726	1.11	34.92	24.40	36.96
F05246+0103	1.15	34.33	24.88	36.36
F05265-4720	1.27	< 34.37	24.60	< 36.41
F06065-7934	-0.19	35.16	26.31	37.19
F06195-4503	-0.24	35.25	25.99	37.29
F08064-1018	-0.51	35.83	25.98	37.86
F09165-0726	0.23	34.40	25.75	36.44
F09323+0732	-0.13	35.91	26.16	37.94
F09416-0137	1.22	34.16	24.60	36.19
F10227-8251	1.07	34.89	24.02	36.92
F10418+1153	0.44	35.21	25.38	37.24
F11243-2244	0.67	35.07	24.94	37.10
F11270+0031	-0.18	35.21	25.85	37.25
F12173-3541	1.28	33.39	24.23	35.42
F12183-1015	0.64	< 34.47	25.39	< 36.51
F14381-3901	0.31	35.83	25.18	37.87
F14501+0639	0.12	35.38	25.89	37.41
F15129+0432	1.05	33.57	24.45	35.60
F15494-7905	-0.56	35.51	26.58	37.55
F15599+0206	-0.67	35.57	26.14	37.60
F16159-0402	1.17	35.04	25.15	37.07
F16431+0217	-0.42	35.25	25.43	37.28
F17345+1124	1.14	36.25	24.65	38.29
F19254-7245	1.76	34.57	24.21	36.61
F20203-5733	-0.44	36.88	26.67	38.92
F20517-5809	0.89	< 34.79	24.90	< 36.82
F21139-6613	1.18	34.83	24.36	36.86
F21309-0726	0.72	34.75	24.33	36.79
F21356-1015	1.00	35.90	24.97	37.93
F21497-0824	1.68	34.91	23.54	36.94
F21511-4606	0.66	35.40	24.61	37.43
F21527-2856	0.20	34.37	25.57	36.41
F22537-6512	0.81	35.97	25.11	38.00
F23002-5828	1.12	34.39	24.65	36.43
F23075-5957	0.66	34.42	25.15	36.46
F23140+0348	-0.35	35.39	26.49	37.43
F23389+0300	0.80	34.84	25.28	36.88
F23400-8705	0.32	34.82	24.73	36.86
F23475-7407	1.08	< 34.40	23.86	< 36.43
F23493-0126	-0.46	35.71	25.99	37.74
F23565-7631	1.13	< 34.26	23.89	< 36.29

## A. Optical Spectra of FIR-Luminous Radio-Excess Objects

Here we show the low-resolution optical spectra discussed in Section 2 (Fig. 14).

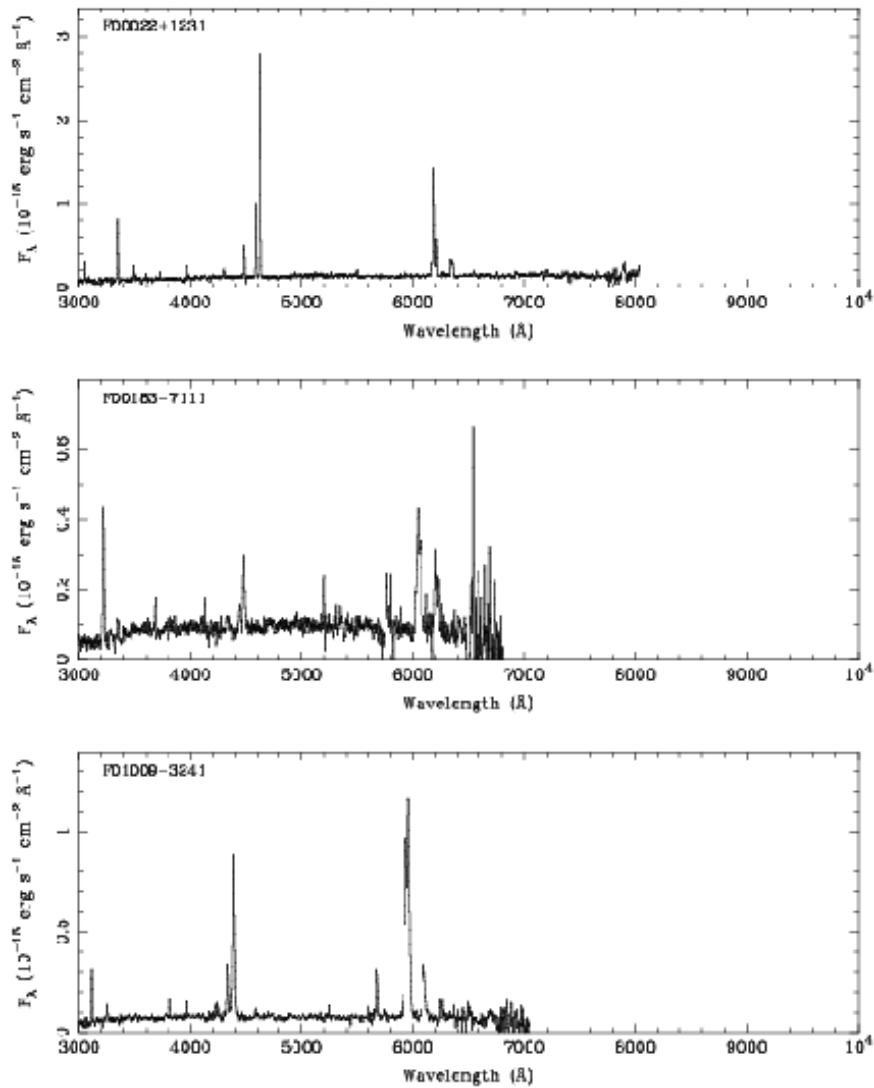


Fig. 14.— Optical spectra of the FIR-luminous radio-excess *IRAS* galaxies. Spectra have been converted to rest-frame. The vertical axis is  $F_\lambda$  in units of  $\text{erg s}^{-1} \text{ cm}^{-2} \text{ \AA}^{-1}$ .

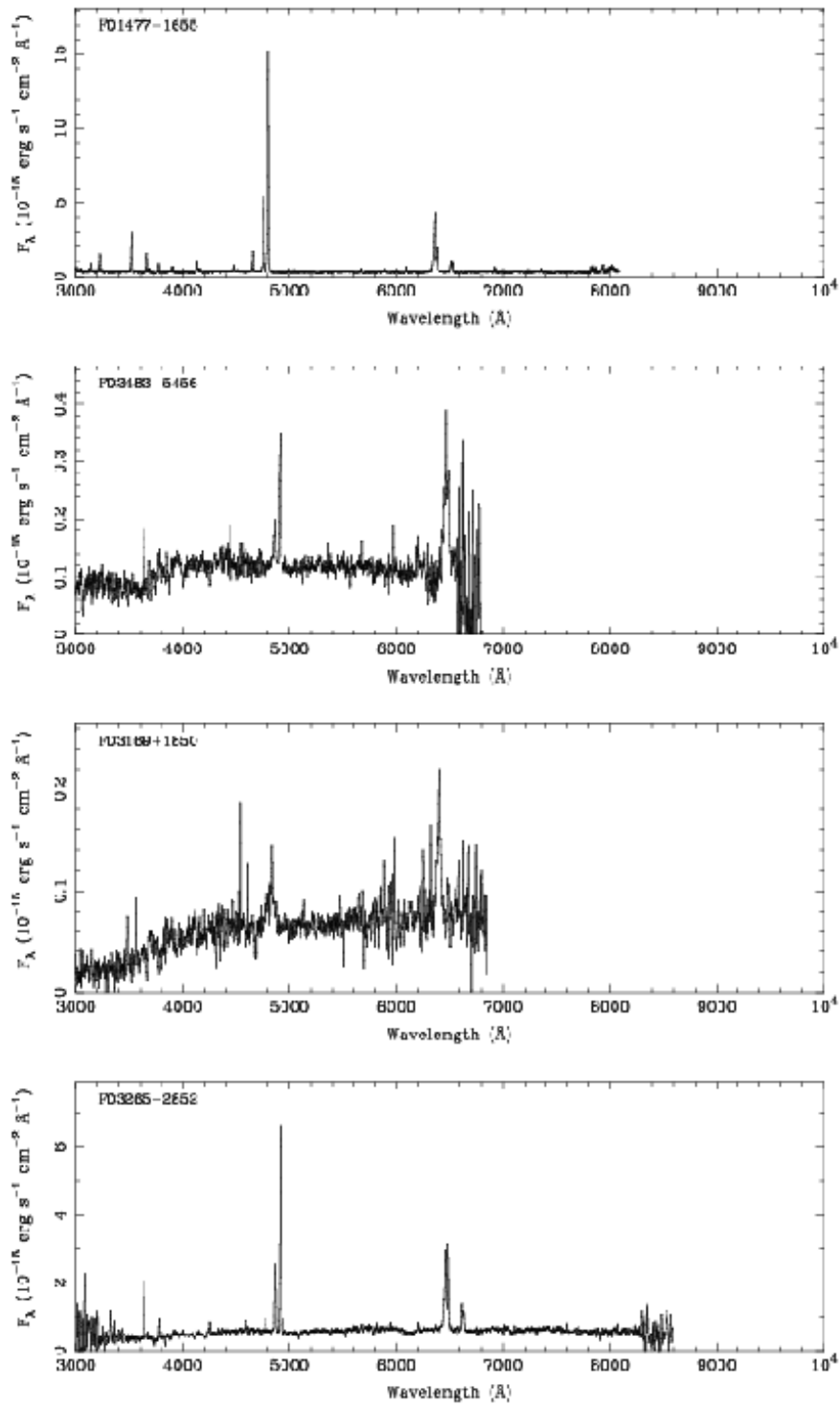


Fig. 14.— *Continued.*

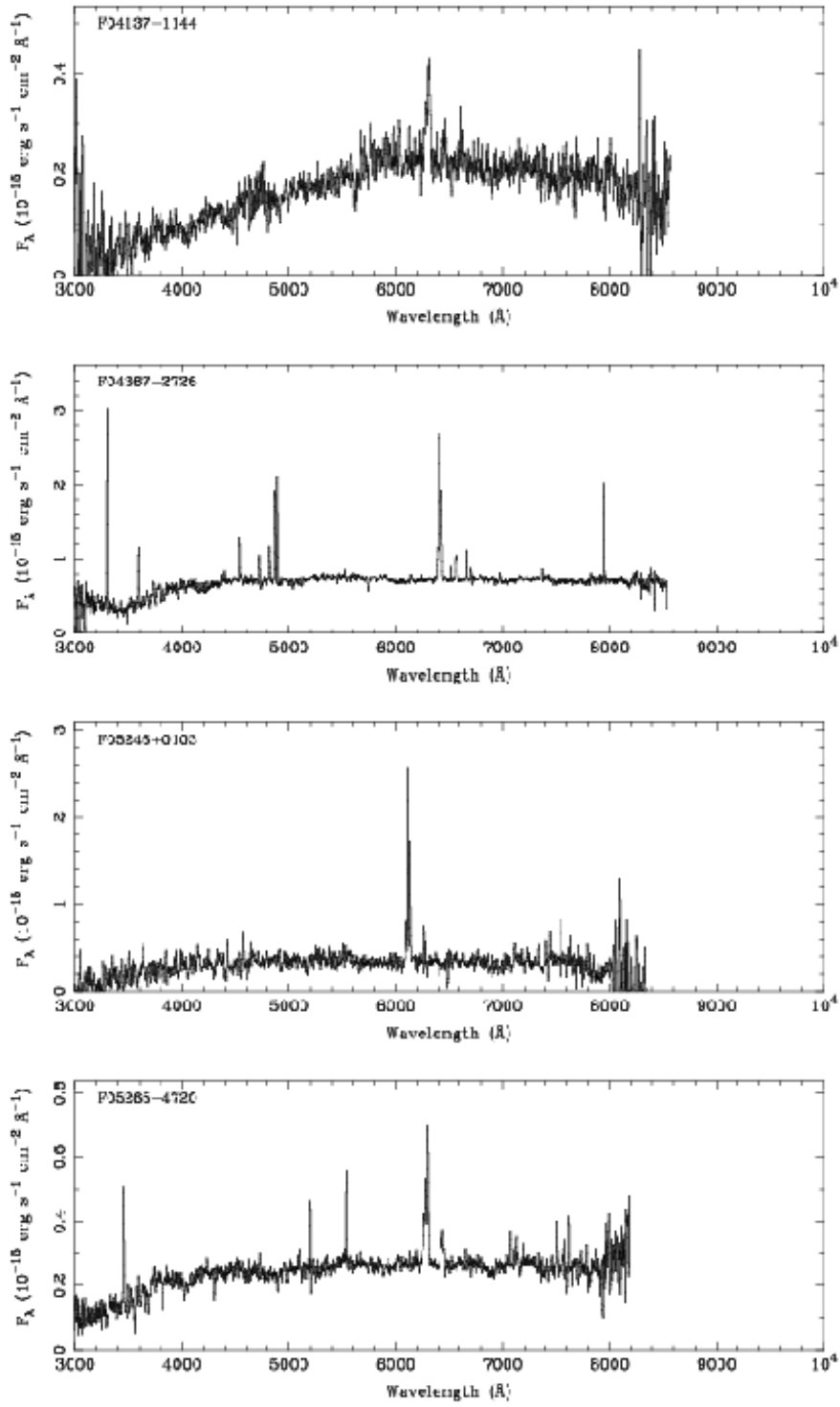


Fig. 14.— *Continued.*

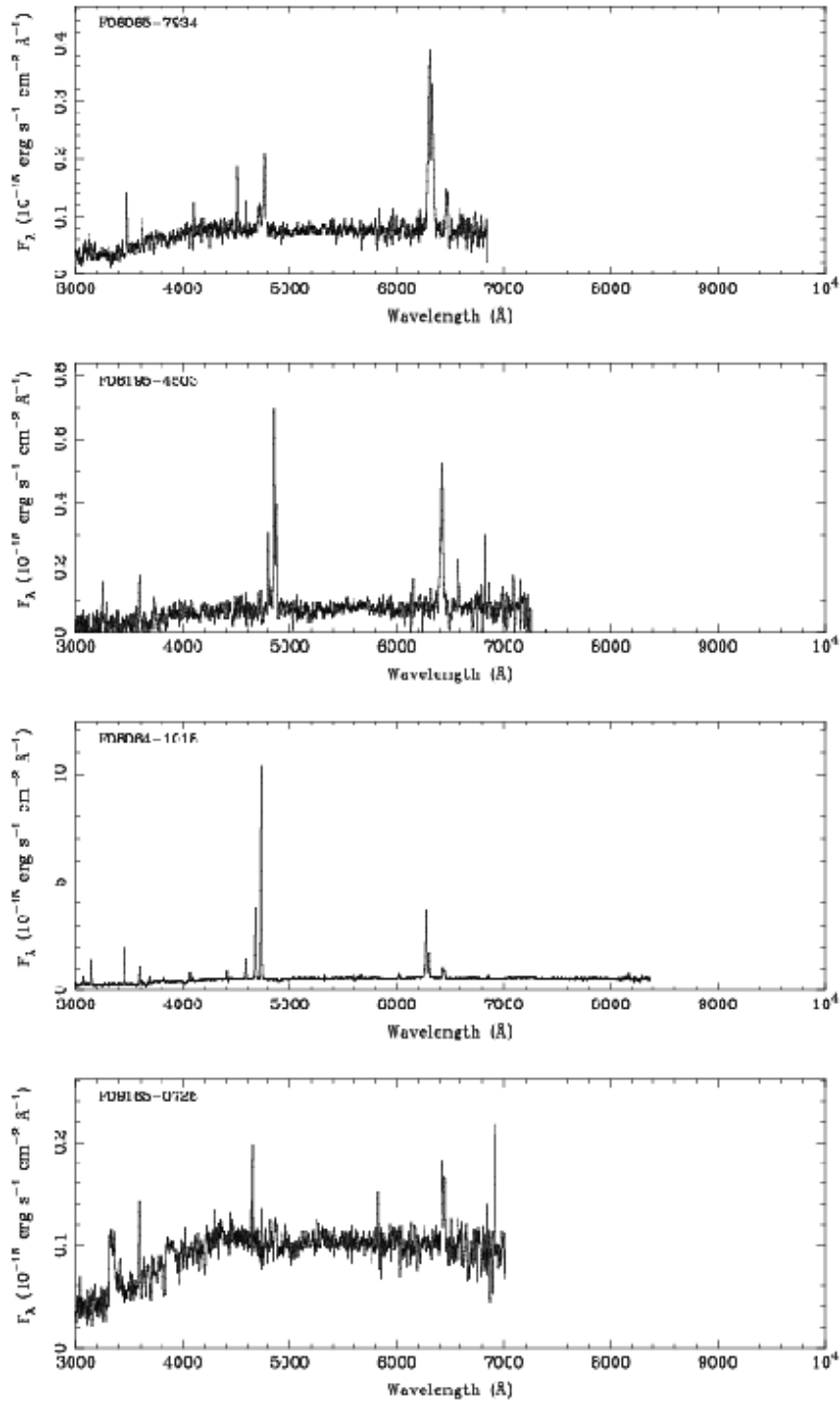


Fig. 14.— *Continued.*

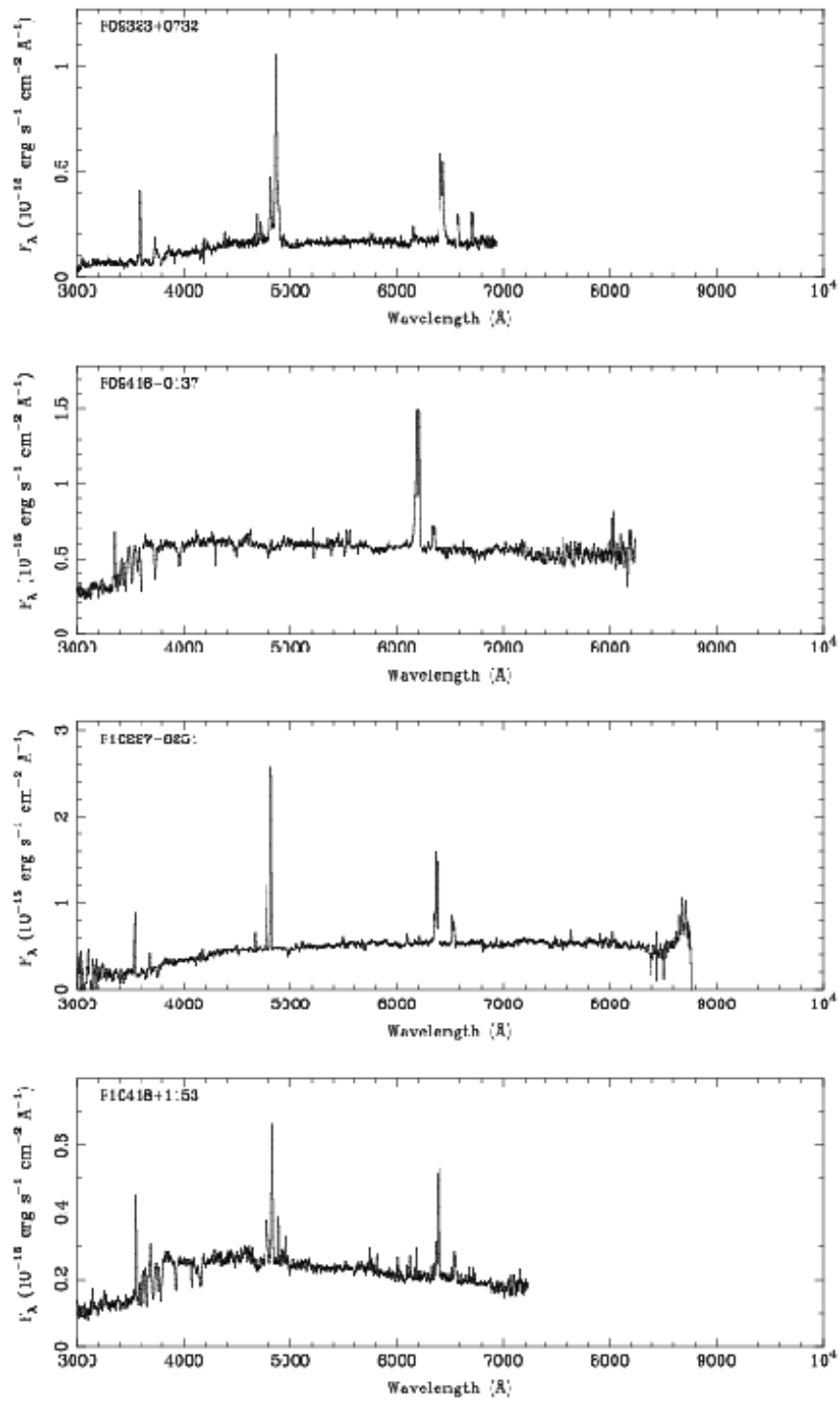


Fig. 14.— *Continued.*

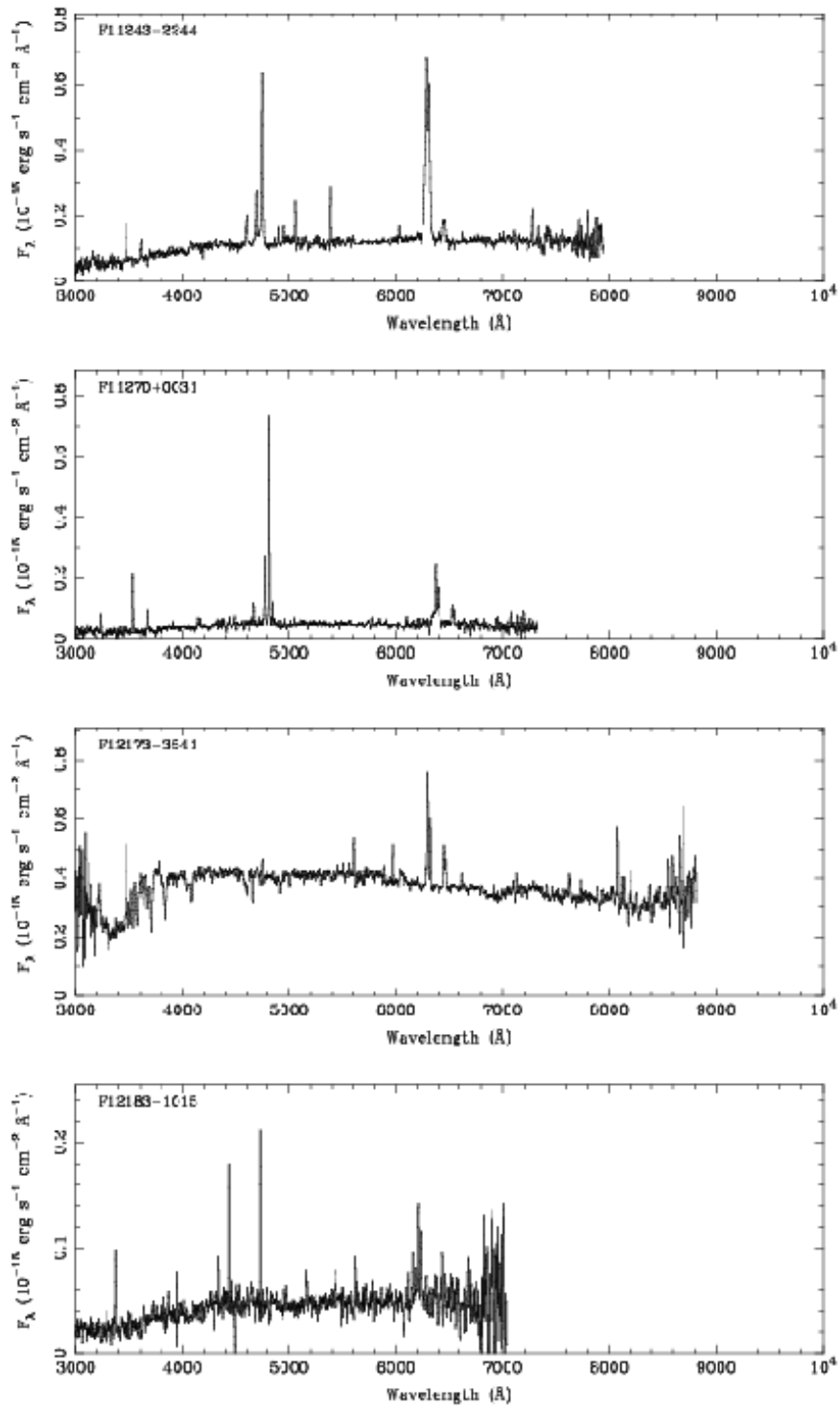


Fig. 14.— *Continued.*

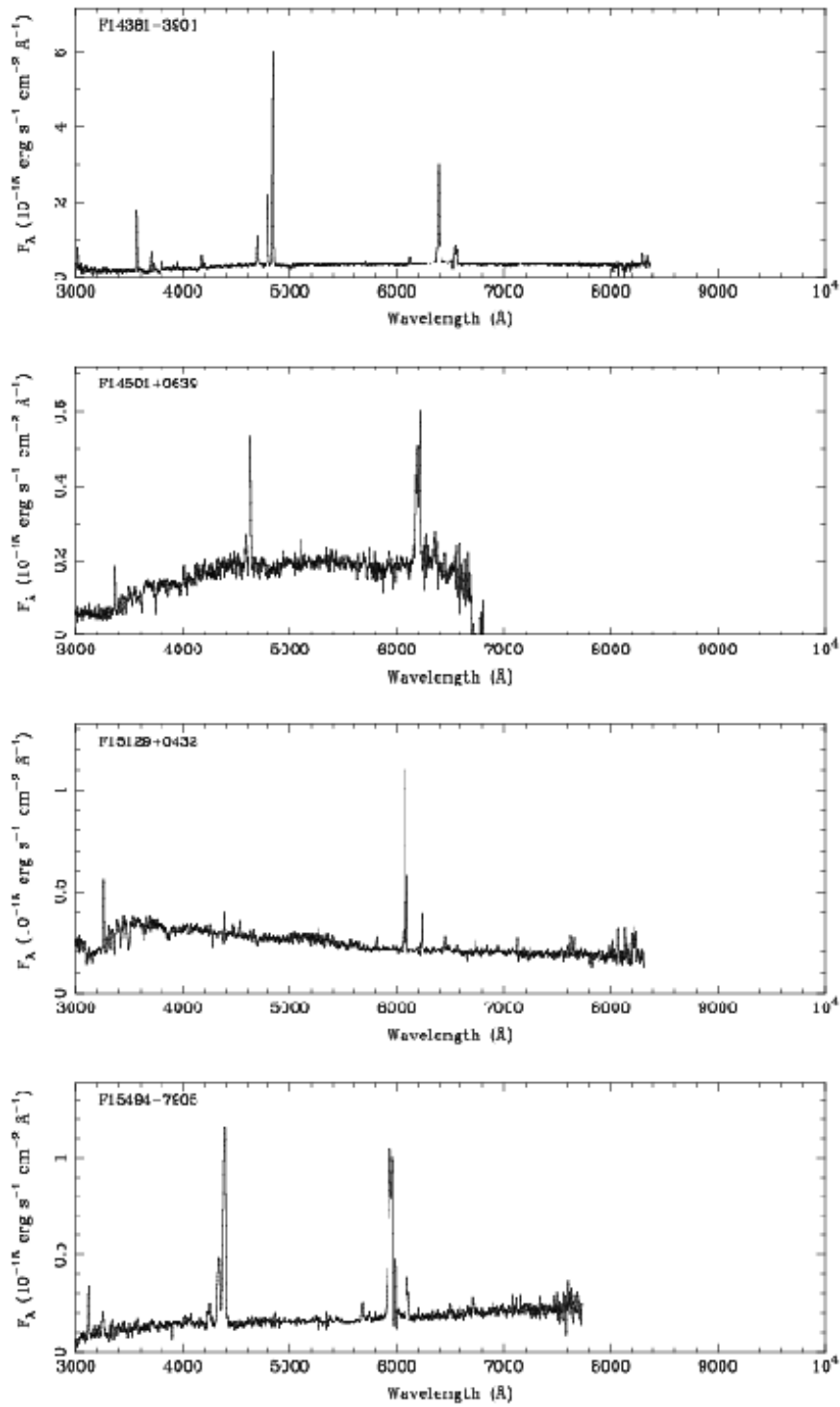


Fig. 14.— *Continued.*



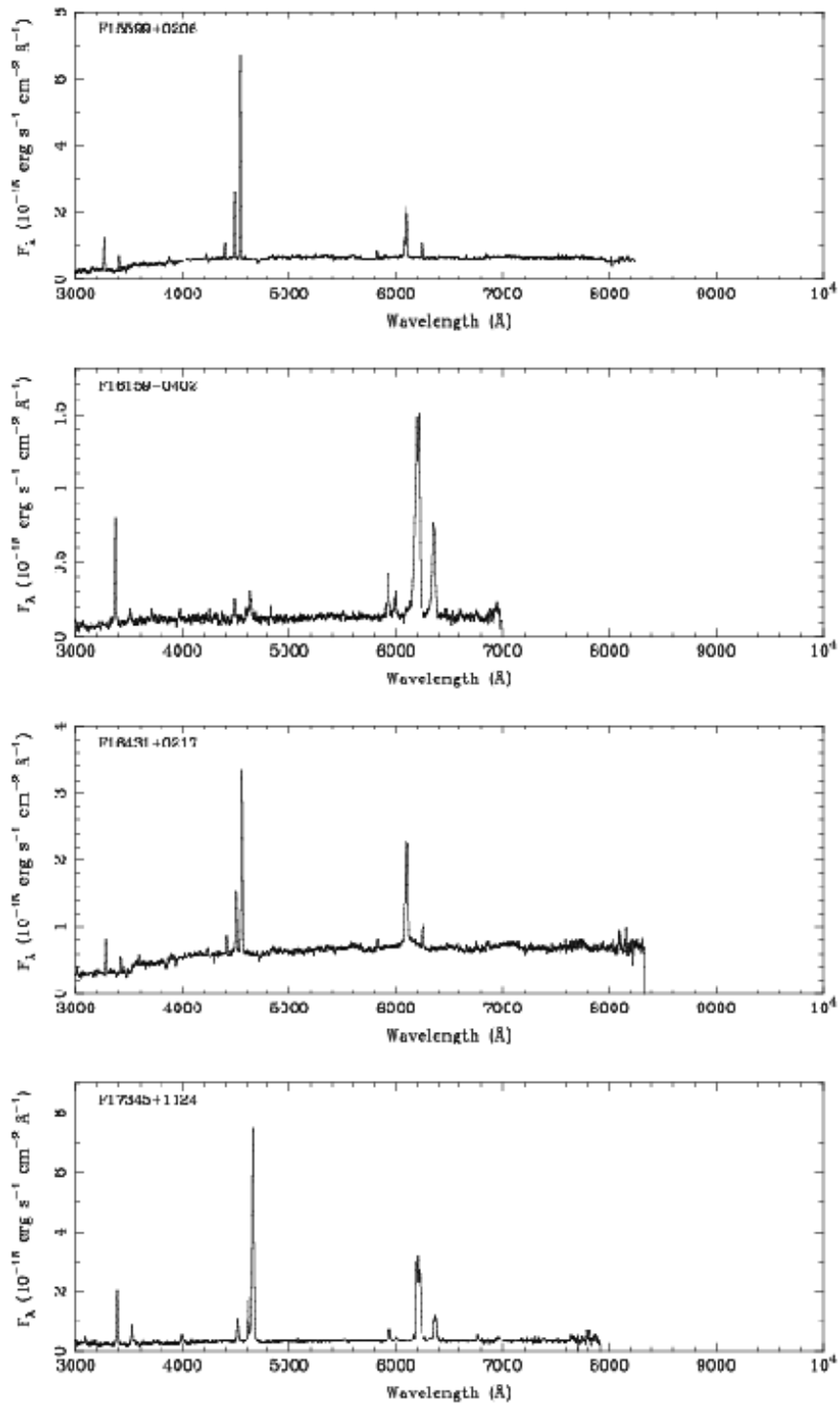


Fig. 14.— *Continued.*

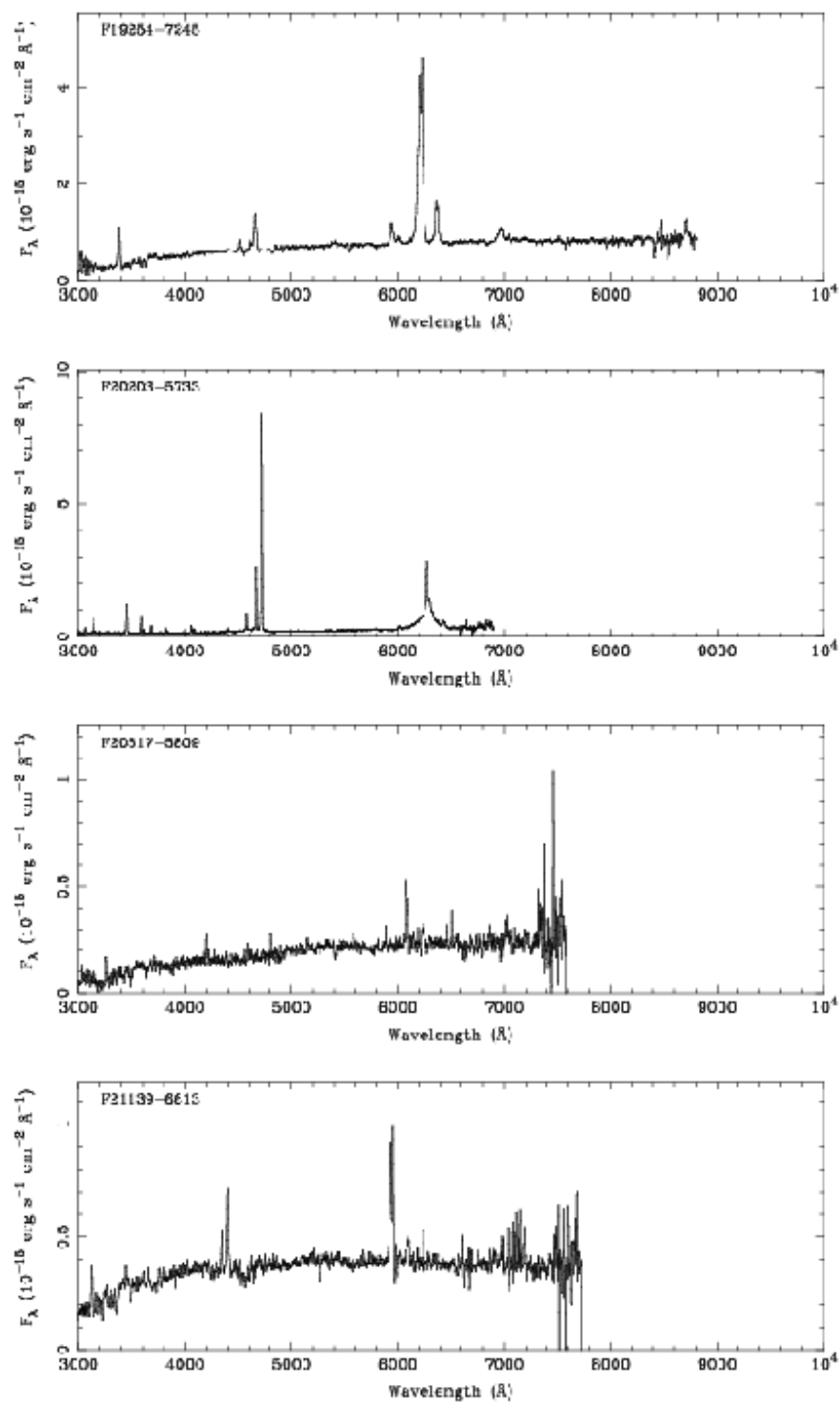


Fig. 14.— *Continued.*

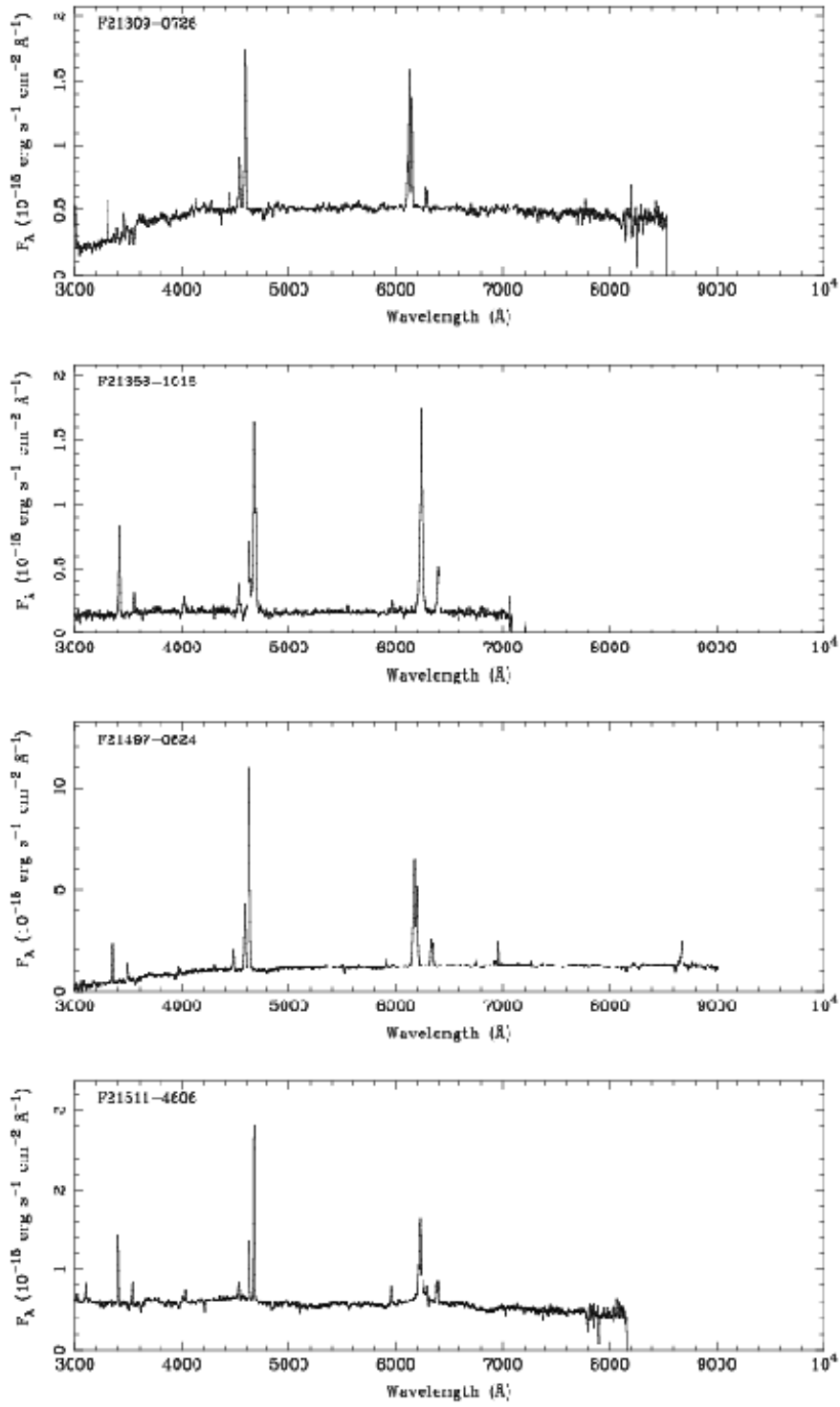


Fig. 14.— *Continued.*

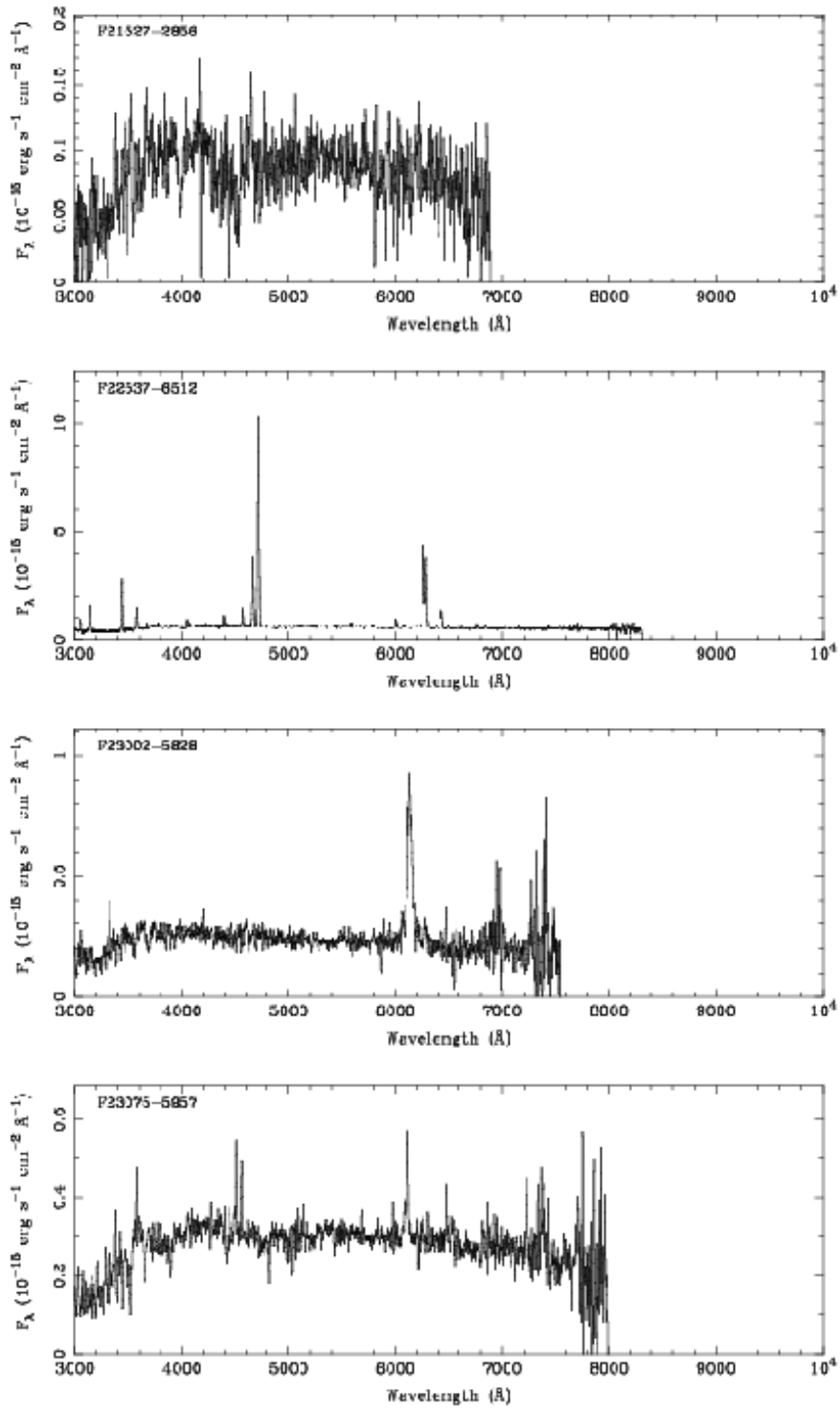


Fig. 14.— *Continued.*

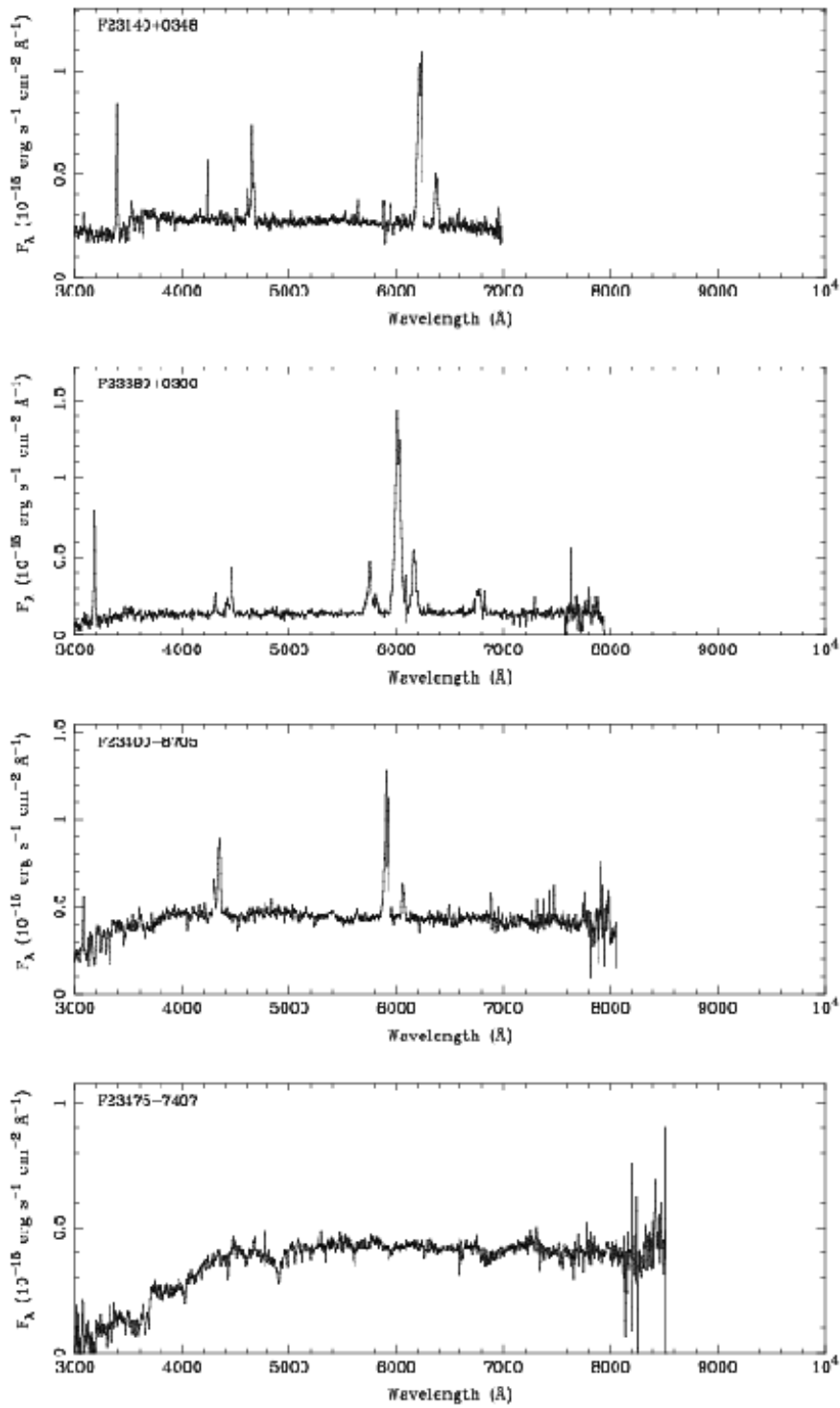


Fig. 14.— *Continued.*

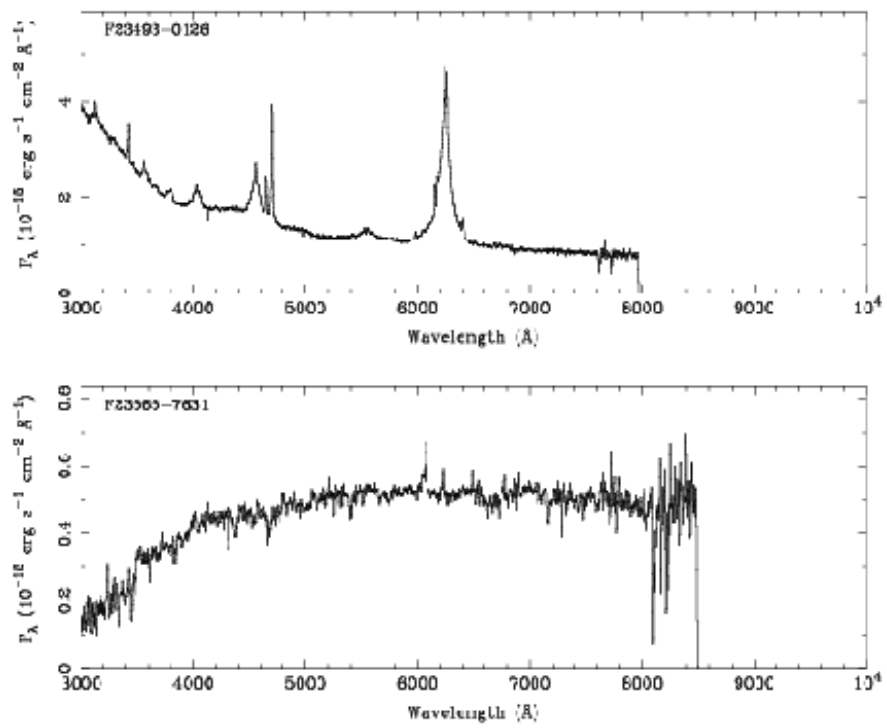


Fig. 14.— *Continued.*